Nonlinear self-consistent theory for crossed-field devices

S. Riyopoulos
Science Applications International Corporation, 1710 Goodridge Drive, McLean, Virginia 22102
(Received 24 August 1992)

A closed, nonlinear set of fluid equations that is based on the electron guiding-center orbits and is generally applicable to the analysis of crossed-field, slow-wave devices, is developed. The equations are used to model the behavior of the crossed-field amplifier. The dielectric response from the spoke charge is self-consistently included. A mean-field approximation is introduced to express the effect of the spoke charge on the rf mode profile. The dielectric modifications are then parametrized by an average amplitude factor $\hat{\Lambda}$ and an average phase shift $\hat{\psi}$ from the vacuum values. In the synchronous with the rf signal frame of reference the streamlines follow the equipotential surfaces of the transformed fields. In the steady state, the flow is incompressible. A uniform-density, constant-height electron hub feeds the current spokes. The secondary electron production at the cathode is computed self-consistently through the secondary-emission coefficient and the average impact energy. The spoke current is determined by the difference of the $E\times B$ drift at the top of the hub from the rf phase velocity. At small space-charge density relative to the Brillouin density, the dielectric corrections enter as a rotation $e^{i\hat{\psi}}$ of the complex growth rate relative to the growth without spoke self-fields. The numerical solutions for arbitrary space charge are compared with previous results without spoke-field effects. An increase in the rf gain and in the anode dc current is observed at any given operation point, despite a small drop in the efficiency. It is concluded that the increase in the rf field strength in the anode-cathode space, caused by the spoke self-field, compensates for the detuning effects from the modifications on the rf mode profile. In reentrant devices, the recycling of the space charge further increases the output power and the level of noise generated by the output-input feedback.

PACS number(s): 52.75.Ms, 52.75.Pv, 85.10.−n

I. INTRODUCTION

Theoretical modeling of microwave crossed-field devices (CFD) must cope with certain complex issues particular to the interaction mechanisms taking place. To begin with, the geometry of the anode structure, supporting the slow wave, complicates the solutions for the cavity-mode profiles. Also, the electron orbits in the combined static and electromagnetic fields are rather complicated, involving several spatial and temporal scales. Second, it must be recognized that these devices usually operate well into the nonlinear regime. The wave-induced *nonlinear* drift of the electron-guiding center bunches the space charge in the anode-cathode space into a characteristic "spoke" structure. The effects of the space-charge fields, both from the presence of an electron sheath around the cathode (hub), as well as the spokes carrying current to the anode, must be included. Third, and perhaps the most destinctive feature for distributed emission CFD's, is the direct coupling of the current source, the secondary-emission cathode, with the physical processes in the interaction space above it. Nonlinear saturation is introduced by the influence of the hub charge on both the secondary emission and the synchronism between the drifting electrons with the wave. Feedback mechanisms are also present in amplifiers with recirculating hub charge, coupling the input with the output.

In a typical magnetron design, each anode slot supports a quasistanding em wave. The slow wave around the cathode can be thought of as the constructive interference among the fringe fields from a sequence of slots. For example, at "π-mode" operation, where the wavelength equals two anode periods (slots plus vanes), approximately one slow-wave length is traveled along the tube within the time the em wave travels back and forth inside one slot. An effective approach of treating the wave propagation is to replace the complicated anode geometry with a smooth anode, and prescribe an equivalent periodic complex impedance [1–3]. One can then impose traveling-wave boundary conditions on the anode, while the cathode is treated as perfect conductor. The dispersion relation is determined by equating the radiation impedance with the anode circuit impedance. An interesting feature of the magnetron is that most of the total wave energy is stored in the "anode circuit", i.e., vane structure, typically more than ten times the circulating energy in the anode-cathode gap. When the hub and the spokes are formed, the power flux in the anode-cathode gap changes significantly, yet the overall energy change is small compared to the energy stored in the anode circuit. The dispersion relation and the boundary conditions at the anode change little from the vacuum values. This allows the description of the nonlinear operation in terms of modified vacuum eigenmodes, of slowly varying complex amplitude, even at high spoke current.

The energy source driving the wave instability is the applied voltage difference across the anode-cathode gap. Electrons emitted from the cathode are accelerated by

the electric field across the gap and start to rotate in the magnetic field. As the average magnetic $\mathbf{v}\times\mathbf{B}_0$ force balances the electrostatic, the center of the electron cyclotron rotation drifts in the $\mathbf{E}_0\times\mathbf{B}_0$ direction along the cathode. The maximum electron excursion from the cathode, about twice the Larmor radius, is less than the anode-cathode distance for applied voltages below the Hall cutoff at given B field (condition for magnetic insulation of the anode). When the electrons are let to interact with a slow wave of phase velocity nearly equal to the dc drift velocity, they may either lose or gain energy, depending on the relative phase with the wave. If the rf interaction tends to decrease the electron velocity, the electrostatic force momentarily exceeds the magnetic, drawing the electrons closer to the anode. The potential energy thus extracted from the dc field serves to maintain the electron drift velocity along the cathode, against the opposing force from the rf field. In this process the wave acts as a drag force, absorbing the energy gained from the electron slow drift across the anode-cathode voltage, in a way preserving the $\mathbf{E}_0\times\mathbf{B}_0$ drift and the synchronism condition. The resulting motion of the electron guiding center (GC) is a composite linear dc drift and a nonlinear rf drift. The rf drift is responsible for the bunching of the electrons in spokes and the current flow to the anode.

Spoke formation (bunching in space) at even modest rf power makes CFD operation inherently nonlinear. Linear perturbation theories, based on small-amplitude periodic excursions about a uniform GC motion, also predict diocotron-type instabilities [4–8] in the electron sheath around the cathode. The unstable modes, triggered by the shear in the drift velocity, can be either slow waves ($v_p/c \ll 1$) in magnetrons [4,5] or fast extraordinary waves ($v_p/c \leq 1$) in smooth anode tubes [6–8]. The linear solutions are singularly localized around some resonant layer inside the hub and do not match the profiles of the CFD excited modes, which are similar in structure to the vacuum cavity eigenmodes. Large signal studies [9–12], on the other hand, have dealt with magnetron-type situations, employing symmetric field structure with identical spokes, and assuming that the resonant condition is unchanged along the tube. However, the variation in the detuning, caused by the hub density evolution and/or the nonlinear phase slippage, is dominant in crossed-field amplifiers (CFA's). In fact, the synchronism condition may change dramatically from spoke cutoff near the input to full spoke width near the output. The rise time for the newly formed spokes at the input must also be considered. These issues have only recently been self-consistently addressed [13,14].

A particular feature of the CFD operation is the insensitivity to thermal spreads. Unlike other microwave devices, such as the electron cyclotron maser and the free electron laser, where the instability is triggered by bunching in the velocity space, CFD instabilities involve bunching in real space, manifested by the spoke formation. The synchronism condition is determined by drift velocity of the GC, which depends only on the local strength of the static fields. Any thermal spreads among the emitted or the injected electrons are distributed in the velocity and the angle of the cyclotron rotation. It will be shown that the wave energy exchange with the cyclotron motion averages out for a uniform gyroangle distribution. Nearly uniform gyroangle distributions are the statistically most probable in CFA's, in the absence of cyclotron resonances causing phase bunching. Two consequences follow. First, the wave-particle energy exchange is determined by the wave-induced shift in the GC position. Second, the gyrovelocity spreads become irrelevant, and efficiencies in excess of 50% are easily and customarily feasible.

A considerable simplification of the CFD theory is possible by utilizing the separation of time scales in the particle motion: in a frame of reference moving near the phase velocity, the cyclotron rotation of an electron proceeds much faster than the shifting of the center of this rotation (guiding-center drift). By averaging the fast, periodic gyromotion out in time, one is left with equations for the motion of the guiding center [11,12]. The guiding-center flow has been recently utilized [13,14] in deriving a closed set of nonlinear equations for the CFA fields and currents. The spoke current flows along the incompressible guiding-center streamlines. A uniform density electron sheath (hub) feeds the base of the spoke. The hub density is determined by the balance between secondary emission and the current drawn. The current through the top of the hub is controlled at each moment by the ratio of the dc field detuning from the synchronous [Buneman-Hartree (BH)] voltage to the rf voltage amplitude. Flux conservation and the flight time for each spoke element determine the current at any given spoke location from the current through the spoke base at previous times. The average electron impact energy on the cathode is found self-consistently from the local dc and rf fields.

While the effects of the hub charge around the cathode have been taken into account [13,14], the fields from the spoke charge itself have so far been neglected. A complete, self-consistent theoretical model, including the effects of the spoke-charge fields, is developed in this paper. The space-charge effects are expressed in terms of the nonlinear dielectric response, obtained in a closed (nonperturbative) form. The exact solution is then utilized to construct "mean-field" solutions for the total fields in the cavity. The profiles of these approximate solutions retain the geometrical similarity with the vacuum cavity modes. Thus they can easily fit in the previously developed formalism while retaining the essential space-charge effects. In this approach, the spoke self-field effects are parametrized by a mean change in the rf voltage amplitude and a mean shift in the rf phase relative to the empty-cavity values for the same boundary conditions.

The physical picture emerging from taking dielectric spoke effects into account remains qualitatively similar to earlier results. The essence of the CFD interaction lies in the variation of the synchronism between the electrons and the wave along the tube, caused by the hub density evolution, the rf phase slippage, and the variation in the spoke topology. The hub density plays the primary role in regulating both the anode current and the production of secondaries. Regulation of the spoke current results

from the modification of the dc field above the hub, which then affects the matching between the $\mathbf{E}_0 \times \mathbf{B}_0$ drift and the phase velocity. The secondary emission is also affected by the hub density, since the impact energy depends on the electric-field strength at the cathode. The spoke-charge effects change the operation characteristics quantitatively. The spoke charge generates its own rf field nearly 90° out of phase from the rf phase at the anode. The self-field generally results in higher field strengths in the anode-cathode space for given anode rf voltage, and in a higher current drawn from the hub. The current flows along the equipotentials of the total rf field in the synchronous frame. Thus the increase in current density is accompanied by a phase shift in the flow pattern from the vacuum mode equipotentials. The combined effect of the spoke charge fields is an overall increase in both the anode current and the rf output power at a given operation point, despite a small decrease in the interaction efficiency. Part of the increase in the output power comes from the spoke charge recycled to the input via the tube drift space in reentrant devices.

The feedback introduced by the space-charge recirculation in the tube drift space is of particular importance in reentrant tubes. The output-input coupling from the reentrant hub charge and spoke remnants is perhaps the main noise-generation mechanism in CFA's. The role of the hub charge recirculation has already been analyzed [15]. The balance between current convection and generation of secondaries causes hub density oscillations along the tube that are fed back into the input. The amplitude of these oscillations becomes large in the case of cathode material with high secondary emission coefficient, and the tube cannot settle to a steady state. The feedback effects are considerably intensified by the recycling of the spoke charge and its self-field. The level of the induced fluctuations in the tube output depends on the relative phase of the reentrant spoke, and the degree of the spoke "debunching" that takes place in the drift space. Thus the amount of circulating charge is closely related to the noise levels in CFA's.

The remainder of the paper is organized in the following manner. The basic geometric and physical assumptions of the model are laid out in Sec. II. Sections III–V deal with the description of the CFD dynamics in the synchronous frame of reference. The theory in these sections extends the earlier GC approach to the problem by replacing the vacuum field profiles with self-consistent, "mean-field" profiles, which include the space-charge effects. The equations for the GC orbits are derived in Sec. III. The fluid equations for the hub charge and the spoke current are obtained in Sec. IV. The description is completed in Sec. V, where the space-charge fields are obtained from the nonlinear Poisson equation and the mean-field approximations are constructed. Section VI returns the discussion in the lab frame, taking advantage of the steady-state condition and the current conservation there. The evolution equations for the rf amplitude and phase are worked out in Sec. VII. The dielectric effects from the spoke self-fields are brought out in Sec. VIII by comparing the complex growth rates with and without spoke charge effects. Numerical results, comparisons with experiment, and conclusions are presented in Sec. IX.

II. OUTLINE OF THE THEORETICAL APPROACH

The geometry for the CFA model is depicted in Fig. 1. A linear, two-dimensional configuration is adopted, neglecting the effects of the curvature and the nonuniformity along the tube axis z. The dc voltage V_{dc} is applied in the x direction across the anode-cathode spacing D, while a uniform magnetic field is applied along z. A single-frequency wave of slowly varying phase and amplitude is considered in our model, given the narrow frequency band characterizing CFA operation at steady state. A truncated Fourier expansion of all the relevant quantities into two components, the dc and the fundamental spatial harmonic only, is used. Since the anode-cathode structure supports slow waves, $v_p/c \ll 1$, the electrostatic approximation $\mathbf{E}(\mathbf{r},t) = -\nabla \mathcal{V}(r,t)$ is adopted for the combined rf and dc fields, $\mathcal{V}(\mathbf{r},t) = \mathcal{V}_0(\mathbf{r}) + \mathcal{V}_1(\mathbf{r},t)$. The potential $\mathcal{V}(\mathbf{r},t)$ obeys Poisson's equation:

$$\nabla^2 \mathcal{V}(\mathbf{r},t) = -4\pi n(\mathbf{r},t) , \tag{1}$$

where $n(\mathbf{r},t)$ includes both the hub and the spoke charge. The simplifying assumption of an electron sheath of constant height d and uniform density n_0 (without a wavelength λ) is made for the cathode hub. This is based on numerical observations showing little change in the hub thickness. Steady-state operation is assumed in the following sense: the rf and dc amplitudes at a given position $\mathbf{r}$ remain invariant in time, while they differ between two positions $\mathbf{r}$ and $\mathbf{r}'$ at any given instant t (amplification along the tube). In other words, an observer at $\mathbf{r}$ always sees an identical spoke repeating at the wave frequency, while two simultaneous observers, separated by an integer number of wavelengths, see a different spoke structure. The incompressibility of the guiding-center flow,

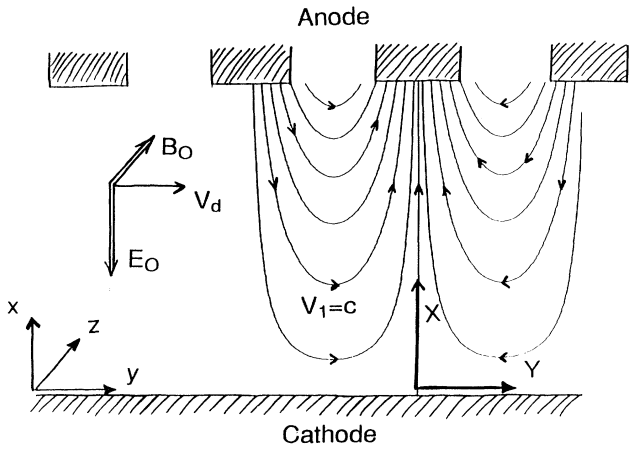

FIG. 1. Simplified illustration of the CFA geometry. The rf equipotentials are also the GC streamlines at perfect synchronism.

shown to be parapotential, and the conservation of the dc current along the streamlines, valid in steady state, offer a further and considerable simplification: it is sufficient to compute the density and current at the base of the spoke to known them everywhere in the interaction space. That reduces the dimensionality of the problem down to one dimension: the distance traveled along the tube.

The single-frequency cavity modes are solutions of Eq. (1) with $n(\mathbf{r},t)=0$ subject to as low wave boundary condition at the anode, $\mathcal{V}_1(x=D,y,t)=-V_1\sin(ky-\omega t)$ and $\mathcal{V}_1(x=0,y,t)=0$ at the cathode,

$$\mathcal{V}(x,y,t)=-\tilde{V}_1\sinh(kx)\sin(ky-\omega t+\phi)\ , \tag{2}$$

where $\tilde{V}_1=V_1/\sinh(kD)$. The above profiles approximate the exact vacuum solutions, having the form of Bloch waves

$$\mathcal{V}(x,y,t)=-\tilde{V}_1 W(x,y)\sinh(kx)\sin(ky-\omega t+\phi)\ , \tag{3}$$

where the function $W(x,y)=1+\sum_{l\neq 0}W_l(x)\exp[il(2\pi/a)y]$ carries the y periodicity of the anode vanes a. The single-frequency eigenmodes of Eq. (3) have a wide wave-number content $k_l=k+l(2\pi/a)$. The reason for dropping terms with $l\neq 0$ from the analysis is that the phase velocities ω/k_l are far from ω/k given that $k\leq 2\pi/a$. Since the $\mathbf{E}_0\times\mathbf{B}_0$ velocity in CFD's is near resonance with ω/k, the $l\neq 0$ terms are out of synchronism and do not contribute to the wave energy exchange with the electrons. The energy exchange determines the complex growth rate $\Gamma(\omega)$, including the wave-number shift from the vacuum dispersion $k(\omega)$. The exact vacuum dispersion, consistent with the full eigenvalue solutions Eq. (3), is assumed, since the $l\neq 0$ terms are essential in determining the vacuum phase and group velocity. Thus, while the contribution from the nonresonant terms is negligible in the wave-particle energy exchange, it is retained in the determination of the synchronism condition and the rf power flux along the tube.

When the rf interaction with the electrons is turned on, the amplitude V_1 and the phase ϕ become slowly varying functions of the traveled distance y along the tube. In addition, the spoke self-fields modify the total field structure. The space charge of a spoke driven by a sinusoidal anode voltage gives rise to both sine and cosine electrostatic components, as well as a dc contribution and smaller higher harmonics. The new rf profile, neglecting harmonics, is given by

$$\mathcal{V}_1'(x,y,t)=-\tilde{V}_1\{[1+\epsilon_1(x)]\sinh(kx)\sin(ky-\omega t) +\epsilon_{-1}(x)\sinh(kx)\cos(ky-\omega t)\}\ . \tag{4}$$

The dielectric components $\epsilon_{\pm 1}(x)$ are obtained from the solution of a nonlinear Poisson equation. In standard notation $\epsilon_{\pm 1}(x)$ are related to the real and imaginary parts of the complex plasma susceptibility χ by $\epsilon_1=\mathrm{Re}\chi/4\pi$, $\epsilon_{-1}=\mathrm{Im}\chi/4\pi$. Note that Eq. (4) can be written as

$$\mathcal{V}_1'(x,y,t)=-\Lambda(x)\tilde{V}_1\sinh(kx)\sin[ky+\psi(x)-\omega t+\phi]\ , \tag{5}$$

where $\psi(x)=\tan^{-1}[\epsilon_{-1}(x)/1+\epsilon_1(x)]$ and $\Lambda(x)=\{[1+\epsilon_1(x)]^2+\epsilon_{-1}^2(x)\}^{1/2}$. The phases ϕ and ψ are of different physical origin. The implied slow evolution of ϕ expresses the departure from the vacuum dispersion relation. Together with the implied change in V_1, they result from the wave particle $\mathbf{J}\cdot\mathbf{E}_1$ interaction and are directly related to the complex growth rate. The phase $\psi(x)$ and the amplitude factor $\Lambda(x)$, on the other hand, are modifications of the vacuum mode profile by the spoke self-fields. Λ and ψ also vary slowly with the traveled distance y because of the space-charge evolution.

The profiles of Eq. (4) or (5) can replace the vacuum modes of Eq. (2) inside the previously developed CFA evolution equations [13,14], yielding together with the nonlinear Poisson equation (1) a closed system including the spoke-charge effects. However, it is more analytically tractable and physically insightful to introduce a *mean-field* approximation, involving appropriately defined constants, $\hat{\Lambda}$ and $\hat{\psi}$:

$$\hat{\mathcal{V}}_1(x,y,t)=-\hat{\Lambda}\tilde{V}_1\sinh(kx)\sin[ky+\hat{\psi}-\omega t+\phi]\ . \tag{6}$$

The mean-field solutions preserve the geometrical similarity between the rf profiles with space-charge effects and the normal mode (vacuum) profiles of Eq. (2). In addition, the spoke-charge effects are described by only two parameters: a mean amplitude boost $\hat{\Lambda}$ and a mean phase shift $\hat{\psi}$. The criterion for obtaining the parameters $\hat{\Lambda}$ and $\hat{\psi}$ is that the approximation Eq. (6) produces GC flow that is "globally" as close as possible to that produced by the exact profile, Eq. (5). Given the $\mathbf{E}\times\mathbf{B}$ nature of the GC motion, $\hat{\Lambda}$ and $\hat{\psi}$ are obtained from the minimization of $\int d^3\mathbf{r}\|\hat{\mathbf{z}}\times(\nabla\mathcal{V}_1'-\nabla\hat{\mathcal{V}}_1)\|/\Omega$ over a wavelength volume element.

The field and orbit computations are simplified by going to the synchronous frame moving at the phase velocity $v_p=\omega/\hat{k}$. In this frame, the wave phase is frozen in time, leaving only the slow variation of the rf amplitude and the charge density. In general, the phase velocity differs from the vacuum value ω/k, since the effective wave number $\hat{k}=k+d\phi/dy$ is modified by the phase slippage resulting from the wave-particle interaction. This departure can be important in determining the wave-particle synchronism. Strictly speaking, v_p is not constant, because $d^2\phi/dy^2\neq 0$. However the inertial force due to the change in v_p is small, and the synchronous frame will be treated as inertial. Once the spoke boundaries and the charge distributions are computed, they are transformed back to the lab frame, where the final evaluation of the evolution equations for the rf signal take place.

III. GUIDING-CENTER ORBITS

The fast-time dependence on the rf frequency is eliminated by going to the synchronous frame, moving at the phase velocity $v_p=\omega/k$, where the Doppler-shifted frequency $\omega'=\omega-kv_p=0$. In that frame, the electron velocity is separated into a slow guiding-center drift and an oscillating gyromotion. The electron position in phase space is expressed in terms of the guiding-center coordinates X, Y, ρ, θ, related to the usual momentum-position

P_x, P_y, x', y' through

$$x' = X + \rho \sin\theta \ , \qquad y' = y + Y + \alpha\rho\cos\theta \ . \tag{7}$$

Above, X and Y denote the location of the guiding center in the synchronous frame having the origin at $y = v_p t$, ρ is the Larmor radius $\rho = v_\perp/\Omega$, $\Omega = |e|B/m_e c$ is the cyclotron frequency, and θ is the gyrophase. The fast-time scale equations for the gyromotion above the hub are

$$\frac{d\theta}{dt} = -\Omega \ , \quad \rho = \text{const} \tag{8}$$

Inside the hub, the gyromotion is affected by the electric-field gradient $dE/dx = m\omega_p^2/e$, where $\omega_p^2 = 4\pi e^2 n_0/m$ is the electron plasma frequency. The gyration becomes elliptical, with the major axis along y and major-to-minor ratio $\alpha = 1/(1-\omega_p^2/\Omega^2)^{1/2}$, while the cyclotron frequency is changed to $\tilde{\Omega} = \Omega/\alpha$.

The gyromotion is averaged out of the exact equation of motion $d\mathbf{p}/dt = -e\nabla\mathcal{V} + e(\mathbf{p}\times\mathbf{B})/m_e C$ by averaging over θ. This calculation has been carried out systematically, using canonical averaging methods elsewhere [16]. Rescaling to dimensionless variables, by normalizing length to k^{-1}, time to ω^{-1}, mass to m_e, charge density to $(m_e\omega^2/|e|)$, voltage to $(|e|/m_e v_p^2)$ and fields to $(k|e|/m_e v_p^2)$, the guiding-center motion $\mathbf{u} = (dX/dt, dY/dt)$ is given by

$$\frac{dX}{dt} = -\frac{1}{\Omega}\frac{\partial}{\partial y}[-\hat{\Lambda}\tilde{V}_1 \sinh X \sin(Y+\hat{\psi}) + \Delta\mathcal{V}_0(X)] + O\left[\frac{V_1^2}{\Omega^2}, k^2\rho^2\right] , \tag{9a}$$

$$\frac{dY}{dt} = \frac{1}{\Omega}\frac{\partial}{\partial X}[-\hat{\Lambda}\tilde{V}_1 \sinh X \sin(Y+\hat{\psi}) + \Delta\mathcal{V}_0(X)] + O\left[\frac{V_1^2}{\Omega^2}, k^2\rho^2\right] . \tag{9b}$$

The term $\Delta\mathcal{V}_0(X) = \mathcal{V}_0(X) - \Omega X$ is the Lorenz transformation (to order v_p/c) of the dc electrostatic potential $\mathcal{V}_0(X)$ in the moving frame, where ΩX is the induced $\mathbf{v}_p\times\mathbf{B}$ voltage. In terms of the synchronous field E_r, corresponding to $\mathbf{E}\times\mathbf{B}$ velocity equal to v_p and given in the dimensionless units by $E_r = -\Omega$,

$$\Delta\mathcal{V}_0(X) = \mathcal{V}_0(X) + E_r X \ . \tag{10}$$

The expressions for $\hat{\Lambda}$, $\hat{\psi}$, and $\mathcal{V}_0(X)$ are given in Sec. V.

Equations (9) are derived from the "averaged" Hamiltonian $H(X,Y)$,

$$\dot{X} = -\frac{1}{\Omega}\frac{\partial H}{\partial Y} \ , \quad \dot{Y} = \frac{1}{\Omega}\frac{\partial H}{\partial X} \ , \tag{11}$$

$$H(X,Y) = -\hat{\Lambda}\tilde{V}_1 \sinh X \sin(Y+\hat{\psi}) + \Delta\mathcal{V}_0(X) \ , \tag{12}$$

Because H is an adiabatic invariant, the trajectories from Eqs. (9) or (11) are given by $H(X,Y) = \text{const}$. Equations (11) can also be written as

$$\mathbf{u} = -\frac{\nabla H \times \hat{\mathbf{z}}}{\Omega} \ , \tag{13}$$

thus H also serves as the stream function for the flow. According to (13), the flow is parapotential, following the equipotential surfaces of the combined transformed potential $H = \mathcal{V}_1(X,Y) + \Delta\mathcal{V}_0(X)$; in particular, when the dc field equals the synchronous field, then $\Delta\mathcal{V}_0 = 0$ and $\mathbf{u}$ is nothing but the $\mathbf{E}_1\times\mathbf{B}_0$ drift in the "frozen" rf field lines in the synchronous frame. The combined velocity $\mathbf{U}$ in the stationary frame is given by $\mathbf{U} = \mathbf{v}_p + \mathbf{u}$. The velocity $\mathbf{U}$ can also be expressed as

$$\mathbf{U} = \mathbf{u}_0 + \mathbf{u}_1 \ , \tag{14}$$

split into the dc drift $\mathbf{u}_0 = c\mathbf{E}_0\times\mathbf{B}/B^2 = \hat{\mathbf{y}}E_0(X)/\Omega = \hat{\mathbf{y}}[v_p - \Omega^{-1}(d/dX)\Delta\mathcal{V}_0]$, and the rf drift $\mathbf{u}_1 = c\mathbf{E}_1\times\mathbf{B}/B^2$. In general $\mathbf{v}_p \neq \mathbf{u}_0$ and $\mathbf{u} \neq \mathbf{u}_1$, because the dc field is neither uniform nor equal to E_r.

The validity conditions for the GC approximation are the existence of a separation in time scales,

$$\frac{k\dot{X}}{\Omega} \sim \frac{k\dot{Y}}{\Omega} \sim \frac{kV_1}{E_r} \ll 1 \ , \tag{15}$$

and the absence of cyclotron resonances

$$kv_d \pm \omega \pm n\Omega \neq 0 \quad \text{for } n \neq 0 \ . \tag{16}$$

The finite Larmor radius effects from the rf field expansion in cyclotron harmonics are of order [16] $J_0(k\rho)I_0(k\rho) \simeq 1 - k^4\rho^4/16$ and are neglected for $k\rho < 1/2$. Also, the quantities V_1 and n_0 must vary slowly, on a time scale much longer than the cyclotron period; that is, if $\tau^{-1} = (d/dt)\ln V_1$, then $\Omega\tau \gg 2\pi$. Finally, terms of order $O(V_1^2)$ or higher are neglected in the right-hand side (rhs) of Eq. (9), implying small V_1 relative to V_{dc}. The quadratic terms $\sim V_1^2$ appear in the guiding-center velocity $\mathbf{u}$ during the fast time averaging [16], and stem from two effects. First, they express a small departure from the parapotential flow because of the inertial force experienced along the curved streamlines. The effect, known in plasma physics as curvature drift, is of order V_1^2/Ω^4. Second, because of the nonlinear phase shift $\phi(y)$, the synchronous frame is not moving at the nominal vacuum phase velocity v_p, but at $v_p' = v_p - d\phi/dy$. Thus the electrons, being in an accelerated frame, experience an additional inertial drift, proportional to $\hat{\mathbf{y}}\times\mathbf{B}_0(dv_p'/dy)$. The above validity conditions are usually satisfied for CFA's.

The trajectories from Eq. (9) are shown in Fig. 1 for no space charge and dc field equal to the synchronous field $E_{\text{dc}} = E_r$. Electrons within $-\pi/2 < Y < \pi/2$ are drawn towards the anode, while the rest are driven back to the cathode. A departure from synchronism $\Delta E_0(X) \equiv -(d/dX)\Delta\mathcal{V}_0(X) = E_0(X) - E_r = 0$, either by detuning the external voltage or by the buildup of space charge, can cause drastic changes in the streamline topology, as demonstrated in Figs. 2(a)–2(d). A boundary curve (separatrix) appears in space, separating trajectories that can reach the anode from those that cannot. The separatrix is the streamline passing through a fixed point

$dX/dt=dY/dt=0$ of the equations of motion, Eqs. (9). Given that $dX/dt=0$ at $Y=\pm\pi/2$ from Eq. (9a), a separatrix emerges when Eq. (9b),

$$\pm\cosh X-\xi(X)=0\ , \tag{17}$$

has solutions for X. The control parameter $\xi(X)$ is the ratio of the detuning $\Delta E_0(X)$ to the normalized rf amplitude $\hat{\Lambda}\tilde{V}_1$. Recalling that the resonant field is related to the phase velocity by $E_r=\Omega v_p$, and taking into account the correction in v_p due to the phase slippage ϕ, $v_p'=v_p-\dot{\phi}$, one has

$$\xi(X)=-\frac{E_0(X)-E_r-\Omega\dot{\phi}}{k\hat{\Lambda}\tilde{V}_1}=\frac{v_d(X)-v_p'}{v_{\rm rf}}\ , \tag{18}$$

where $v_{\rm rf}\equiv k\hat{\Lambda}\tilde{V}_1/\Omega$. The topology of the cross-field flow depends on the number of roots of Eq. (18). Graphic solutions of this equation, showing the intersections of the curves $\xi(X)$ with $\pm\cosh X$, are depicted in Fig. 3 for four typical cases. The following possibilities exist:

(a) No solution, in case of no intersection, curve (a), Fig. 3. The corresponding streamline portrait is shown in Fig. 2(a). There is no separatrix and the flow is similar to the synchronous case $\xi(X)=0$ (unrestricted motion to the anode).

(b) One intersection either with the curve $-\cosh X$ or with the curve $\cosh X$ at $X=S_1$, curve (b), Fig. 3. The corresponding topology is shown in Fig. 2(b). One separatrix curve emerges passing through the unstable fixed point Q_1 at $(Y=-\pi/2,X=S_1)$ or $(Y=\pi/2,X=S_1)$, respectively.

(c) Two intersections with the curve $\cosh X$ at $X=S_1$ and $X=S_0$, curve (c), Fig. 3. The streamline topology is shown in Fig. 2(c). One separatrix curve passes through the unstable fixed point Q_1 at $(Y=\pi/2,X=S_1)$ defines an island centered around the stable fixed point Q_0 at $(Y=\pi/2,X=S_0)$.

(d) Two intersections with $\cosh X$ and one with $-\cosh X$, curve (d), Fig. 3. The topology is shown in Fig. 2(d). Two separatricies emerge, passing through the unstable fixed points, Q_2 at $(Y=-\pi/2,X=S_2)$, and Q_1 at $(Y=\pi/2,X=S_1)$, respectively. An island forms inside

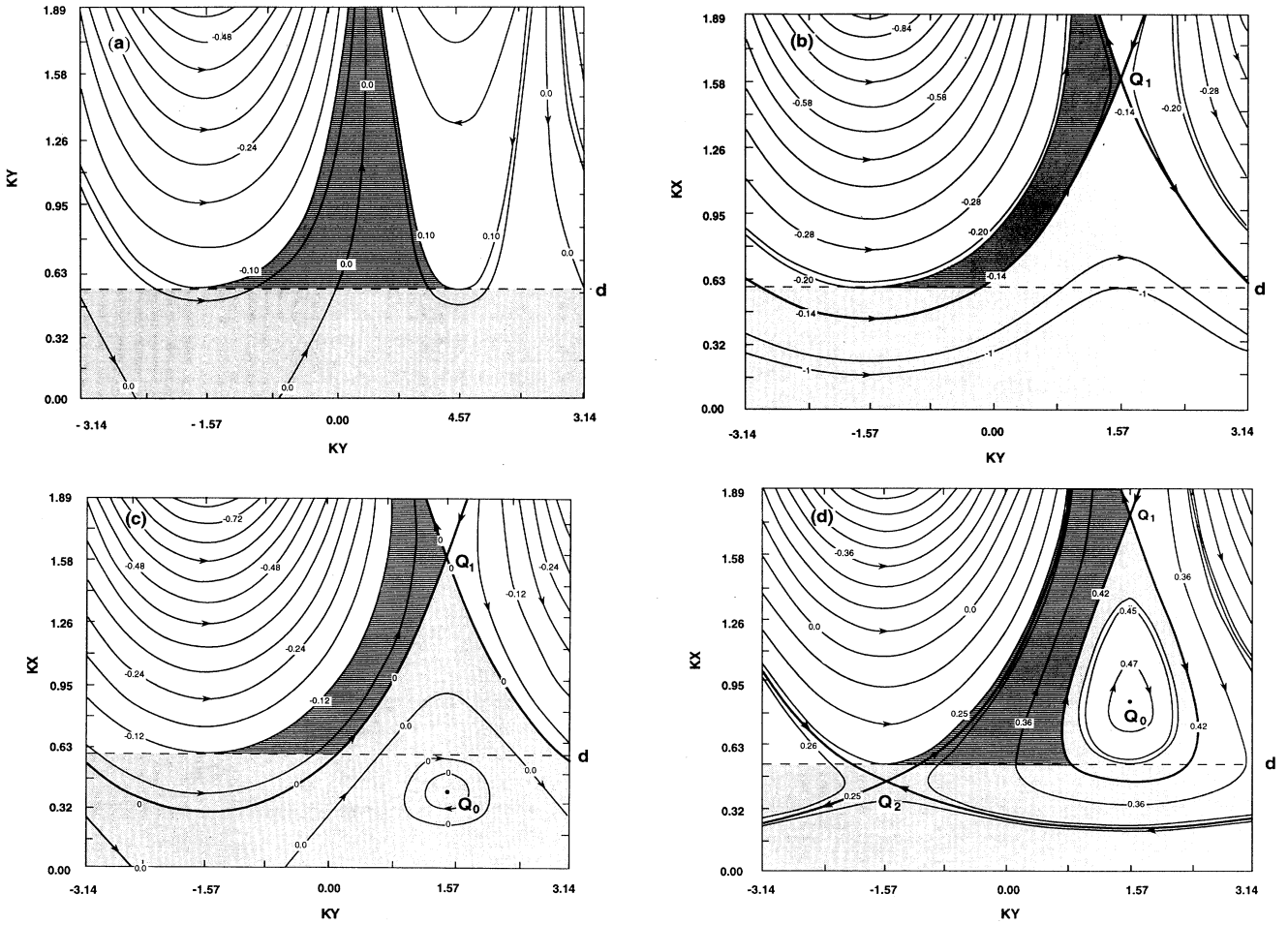

FIG. 2. Guiding-center streamlines in the synchronous frame; (a) $V_{\rm dc}=4.50$, $V_1=0.40$, $n_0=0.060$, $n_s=0.015$; (b) $V_{\rm dc}=4.85$, $V_1=0.40$, $n_0=0.040$, $n_s=0.010$; (c) $V_{\rm dc}=4.75$, $V_1=0.40$, $n_0=0.100$, $n_s=0.025$; (d) $V_{\rm dc}=4.50$, $V_1=0.60$, $n_0=0.500$, $n_s=0.150$. In all cases $\Omega=2.29$ and the hub height $d=d_B$.

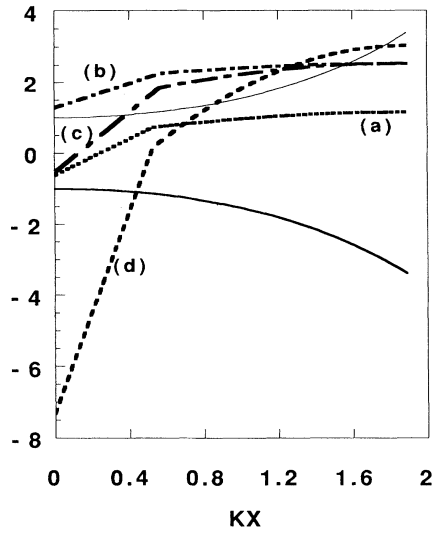

FIG. 3. Graphic solution of Eq. (17) with solid lines for $\pm\cosh X$ and dashed lines for $\xi(X)$. The curves (a)–(d) correspond to Figs. 2(a)–2(d), respectively, representing typical examples of the topologies (a)–(d) discussed in Sec. III.

the spoke around the stable fixed point Q_0 at $(Y=\pi/2, X=S_0)$.

The topology changes continuously as the space-charge density and the rf voltage evolve along the tube. If, for example, one starts from a case of perfect synchronism and no space charge, then $\xi(X)=0$ everywhere. As space charge builds up, $E_0(X)$ falls below E_r inside the hub and ξ becomes negative for $x<d$. At the same time, ξ becomes constant and positive above the hub. This is a consequence of keeping the integral $\int_0^D dX E_0(X)=V_{\rm dc}$ constant: a depression of E_0 inside the hub must be accompanied by an increase of E_0 in the vacuum, in such a way that equal areas are created above and below the line $\xi=0$. The changes in topology are gradual and do not lead to discontinuities in the spoke width.

The emergence of the separatrix has two important consequencies. First, it regulates the current reaching the anode by limiting the width of the spoke; only trajectories passing between Y_1 and Y_2 [heavily shaded areas in Figs. 2(a)–2(d)] can reach the anode. The width of the current channel depends on the number of fixed points and their location relative to the anode and the hub top. In case of one separatrix with the fixed point $S_{1,2}$ below the anode, the minimum distance of the separatrix from the cathode S_m must not exceed the hub height d to have current flowing to the anode. Applying Eq. (12), $H(X,Y)=\text{const}$, along the streamline passing through Q_1, Fig. 2(b), one finds

$$S_m=\xi(\cosh^{-1}\xi-S_m)-\sqrt{\xi^2-1}\ . \tag{19}$$

Second, the center of the spoke is shifted from $Y=0$ towards $Y=\pm\pi/2$. This increases the out-of-phase component of the current relative to the rf field, generating a phase shift $d\phi/dt$, equivalent to a change in the rf wave number, from the cold tube value $k(\omega)$ to $k'=k(\omega)+\dot{\phi}$.

In conclusion, the width of the spoke carrying current to the anode is a function of the ratio $\Delta E_0(X)/k\tilde{V}_1$, where $\Delta E_0(X)=E_0(X)-E_r$ is the departure of the vacuum field from the synchronous field, $E_r=-V_{\rm BH}/D$, corresponding to $v_d=v_p$.

IV. FLUID EQUATIONS

We adopt the picture of a guiding-center fluid, where all the currents are associated with the drift motion of the guiding center. It will be shown that the part of the current associated with the cyclotron motion, and thus neglected in the guiding-center approximation, has a zero contribution to the energy exchange with the wave $\langle \mathbf{J}\cdot\mathbf{E}_1\rangle$. The charge and current density are first obtained in the synchronous frame, where the wave oscillation is frozen and all quantities evolve on the slow time scale. The GC streamlines include the spoke-charge effects.

A. Hub charge density

Inside the hub, the guiding-center flow (9) is not a good approximation for the orbits. For densities near the Brillouin density, the drift velocity near the cathode is much smaller than v_p. This shows as a backstreaming with $k\dot{Y}\sim\omega$ in the moving window, violating the time-scale separation. Also, the streamlines are interrupted by collisions at the cathode, which acts both as a source and a sink. The detailed motion deep in the hub can be neglected as long as the average density can be estimated from the fluxes on the top and bottom of the hub. A uniform density $n(X,Y;y)=n_0(Y)$ is assumed inside the hub $X<d$. The rate of change of n_0 is determined by the balance between electron production via secondary emission and electron convection out of the hub through the current spoke. Secondary electrons are both with their guiding center located at $X\le\rho_0=E_c/\Omega^2$. Therefore, they will strike the cathode again within one cyclotron period if their guiding center falls within $\pi/2<Y<3\pi/2$. Particle simulations have indeed shown that the overwhelming majority of the impacting electrons have an "age" of one cyclotron period. The impact rate, within a section of the tube a wavelength long, is then given by $\pi d n_0 \nu$, where the collision frequency $\nu=\tilde{\Omega}/2\pi$. It yields a production rate of $\pi d n_0\tilde{\Omega}(\delta-1)/2\pi$, where the emission coefficient $\delta(\varepsilon_i)$ is determined from the impact energy ε_i. The rate of loss is given by the current $I_0\equiv I_x(X=d)$ through the base of the spoke. Therefore, the density evolution equation in the lab frame is

$$v_p\frac{\partial}{\partial y}n_0(y)=\frac{\frac{1}{2}n_0 hd\tilde{\Omega}(\delta-1)-I_0}{2\pi hd}\ , \tag{20}$$

given that at steady state $d/dt=v_d\partial/\partial y$. The secondary-emission coefficient δ depends on the dc cathode field E_c and the rf voltage V_1 through the impact energy ε_i. The following semiempirical formula [17] is used:

$$\delta(\varepsilon_i)=\delta_m\left[\frac{\varepsilon_i}{\varepsilon_m}\exp\left[1-\frac{\varepsilon_i}{\varepsilon_m}\right]\right]^{\zeta}, \tag{21}$$

where δ_m is the maximum value at impact energy ε_m and $\zeta\simeq\frac{2}{3}$. The average impact energy in the Lab frame ε_i, computed in Appendix A, is given by

$$\varepsilon_i=4\frac{|E_c|}{\Omega^2}\tilde{V}_1\sinh(k\rho_c), \tag{22}$$

where ρ_c is the electron cyclotron radius at the cathode.

B. Spoke flow

Above the hub, $X>d$, the electrons follow the guiding-center trajectories, Eqs. (12). According to (13), the parapotential flow is incompressible:

$$\nabla\cdot\mathbf{u}=-\nabla\cdot\frac{\nabla H\times\mathbf{z}}{\Omega}=0. \tag{23}$$

Using (23) inside the charge-conservation equation, $\partial n/\partial t+\nabla\cdot n\mathbf{u}=0$, it follows that the total (convective) derivative of the charge density inside the spoke is zero:

$$\frac{dn}{dt}\equiv\frac{\partial n}{\partial t}+\mathbf{u}\cdot\nabla n=0. \tag{24}$$

Thus the density $n(X,t)$ in the spoke position X at time t is simply the hub density $n_0(t-\tau)$ at time $t-\tau(\Delta X,\Delta Y)$, where τ is the flight time for a fluid element to go the distance $\Delta X=X-d$, $\Delta Y=Y-Y_0$. Defining the retarded position

$$\bar{y}(X)=y-v_p\tau(X) \tag{25}$$

in the stationary frame, one has $n(X,Y;y)=n_0(y-v_p\tau)$. It is therefore sufficient to know the hub density at previous locations to find the spoke density everywhere in the interaction space,

$$n(X,Y;y)\equiv\left.\begin{cases}n_0(y), & X<d,\\ n_0(\bar{y}(X)), & \hat{Y}_1(X)<Y<\hat{Y}_2(X),\\ 0, & \text{elsewhere},\end{cases}\right\},X>d, \tag{26}$$

where $\hat{Y}_{1,2}(X)$ are the spoke boundaries. The current density in the synchronous frame, ignoring the cyclotron contribution, is $\mathbf{J}(X,Y)=n(X,Y)\mathbf{u}$, with n given by Eq. (26).

V. SPACE-CHARGE FIELDS

The theoretical description is completed with the evaluation of the hub-charge and the spoke-charge contributions, which are derived from the previously obtained spoke profiles. The spoke self-field changes the structures of both the dc and rf components of the electric fields inside the anode-cathode space quite significantly. However, it can be argued that the effect on the form of the boundary conditions at the anode is small. Most of the wave power flux is supported by the anode circuit, the propagation characteristics of which are independent of the charge in the anode-cathode gap. The change in the dispersion relation and the field profiles inside the slow wave structure is small, even when the spoke self-fields are comparable to the vacuum fields in the anode-cathode space. Thus, at any given operation frequency ω, the boundary condition at the anode (i.e., vane tips) is still approximated by a single sinusoidal slow wave:

$$\mathcal{V}_1(D,y,t)=-V_1\sin(ky-\omega t+\phi). \tag{27}$$

The space-charge contributions alter the field profiles in the anode-cathode gap away from the vacuum profiles obtained under the same boundary condition (27). The field modifications, in turn, affect the rates of the slow amplitude variation dV_1/dy and the phase slippage $d\phi/dy$, computed from the $\mathbf{J}\cdot\mathbf{E}$ average over a wavelength-long slice of the anode-cathode space. Self-field evaluation proceeds in two steps. Exact expressions for the dc and rf spoke-field contributions are obtained in the first subsection. The mean-field approximations are then extracted in the next subsection.

A. Poisson's equation

The Poisson equation for the total potential $\mathcal{V}$ in the synchronous frame is

$$\nabla^2\mathcal{V}=-4\pi n, \tag{28}$$

where n includes both the hub- and the spoke-charge density. Taking the Fourier transform in the Y direction and letting $V(X,Y)=\sum\mathcal{V}'_m(X)\sin(mY)+\mathcal{V}'_{-m}(X)\cos(mY)$, one has

$$\frac{d^2}{dX^2}\mathcal{V}_0(X)=-4\pi n_0(X), \tag{29}$$

$$\frac{d^2}{dX^2}\mathcal{V}'_{\pm m}(X)-m^2\mathcal{V}'_{\pm m}(X)=-4\pi n_{\pm m}(X). \tag{30}$$

Henceforth, the subscript $(+)$ signifies the in-phase (sine) and $(-)$ out-of-phase (cosine) components. The Fourier components of the spoke charge are given by

$$\begin{aligned}n_0(X)&=\frac{1}{2\pi}\int_{\hat{Y}_1(X)}^{\hat{Y}_2(X)}dY\,n_0(\bar{y}),\\ n_{\pm m}(X)&=\frac{1}{\pi}\int_{\hat{Y}_1(X)}^{\hat{Y}_2(X)}dX n_0(\bar{y})\times\begin{cases}\cos(mY)\\ \sin(mY)\end{cases}.\end{aligned} \tag{31}$$

The dc component of the space charge is equal to the uniform hub density n_0 for $X<d$, and to the average spoke density for $d<X<D$,

$$n_0(X)=\begin{cases}n_0, & X<d\\ \dfrac{1}{2\pi}n_0(\bar{y})[\hat{Y}_2(X)-\hat{Y}_1(X)], & X>d,\end{cases} \tag{32}$$

where $n_0(\bar{y})=n_0[y-v_p\tau(X)]$ is the time-retarded hub density, according to the earlier discussion. Substituting in (29), one obtains the dc field

$$-\mathcal{V}_0(X)=\begin{cases}E_cX+2\pi n_0X^2\ , & X<d\\ E_cX+4\pi n_0 d\left[X-\dfrac{d}{2}\right]-\delta\mathcal{V}_0(X)\ , & X>d\ ,\end{cases} \tag{33}$$

where

$$-\delta\mathcal{V}_0(X)=4\pi\int_d^X dX'\int_d^{X'}dX''n_0(X'')\ . \tag{34}$$

The cathode field $E_c\equiv E_x(0)$ is determined from the condition $\mathcal{V}_0(D)=V_{\rm dc}$.

The anode circuit does not support higher harmonics $|m|>1$ and is driven by a sinusoidal input signal. In the synchronous frame, the boundary conditions for the rf field at the anode are $\mathcal{V}'(D,Y)=-V_1\sin Y$. Thus, the Fourier components of (30) are subject to the following boundary conditions: $\mathcal{V}'_1(0)=0$, $\mathcal{V}'_1(D)=V_1$, $\mathcal{V}'_{-1}(0)=\mathcal{V}'_{-1}(D)=0$ and $\mathcal{V}'_{\pm m}(0)=\mathcal{V}'_{\pm m}(D)=0$ for $m\neq 1$. Although the space-charge-induced field harmonics and out-of-phase components are finite in the interaction space, their amplitudes vanish both at the anode and the cathode.

The solutions of (30) can be written as a combination of the homogeneous and nonhomogeneous parts,

$$\mathcal{V}'_m=\mathcal{V}_m+\delta\mathcal{V}_m\ , \tag{35}$$

respectively. The homogeneous solution $\mathcal{V}_m$ subject to the anode boundary condition yields the vacuum mode profile $\mathcal{V}_1(X)=-(V_1/\sinh D)\sinh X\sin Y$. The nonhomogeneous part $\delta\mathcal{V}_m$ yields the spoke self-field that contains both in- and out-of-phase terms relative to the applied rf input voltage,

$$-\delta\mathcal{V}_{\pm m}(X)=4\pi\int_0^D dX'n_{\pm m}(X')G_m(X,X')\ . \tag{36}$$

The relevant charge densities inside (36) are

$$\begin{aligned}&n_{\pm m}(X)=0\ , \quad X<d\ ,\\ &\left.\begin{matrix}n_m(X')\\ n_{-m}(X')\end{matrix}\right\}=\frac{1}{\pi m}n_0[\bar{y}(X')]\times\left\{\begin{matrix}-\cos[mY_2(X')]+\cos[mY_1(X')]\\ \sin[mY_2(X')]-\sin[mY_1(X')]\end{matrix}\right\}\ , \quad X>d\ .\end{aligned} \tag{37}$$

The Green's function

$$G_m(X,X')=\frac{\sinh(mX_<)\sinh[m(D-X_>)]}{m\sinh(mD)}\ , \tag{38}$$

where $X_<\equiv\min(X,X')$, $X_>\equiv\max(X,X')$, satisfies $G_m(0,X')=G_m(D,X')=0$, to comply with $\delta\mathcal{V}_m(0)=\delta\mathcal{V}_m(D)=0$, i.e., to preserve the boundary conditions at the anode and the cathode.

The complete solutions (36) then yield

$$\mathcal{V}'_1(X,Y)=-\tilde{V}_1\sinh X\{[1+\epsilon_1(X)]\sin Y+\epsilon_{-1}(X)\cos Y\}\ , \tag{39}$$

with the dielectric response elements defined by

$$\begin{aligned}\epsilon_{\pm1}(X)&\equiv\frac{\delta\mathcal{V}_{\pm1}(X)}{\tilde{V}_1\sinh X}\\ &=-4\pi\frac{\sinh D}{V_1\sinh X}\int_0^D dX'G_1(X,X')n_{\pm1}(X')\ .\end{aligned} \tag{40}$$

The in-phase dielectric response can be either negative (shielding of the rf potential) or positive (reinforcing), depending on whether the spoke is centered around $\pi/2$ or $-\pi/2$, respectively. A null contribution results for a spoke centered around $Y=0$ (exact synchronism). The opposite is true for the out-of-phase dielectric response $\epsilon_{-1}(X)$. Equation (39) is recast in the form

$$\mathcal{V}'_1(X,Y)=-\Lambda(X)\tilde{V}_1\sinh X\sin[Y+\psi(X)]\ , \tag{41}$$

where the amplitude factor is related to $\epsilon_{\pm1}(X)$ by $\Lambda(X)=\{[1+\epsilon_1(X)]^2+\epsilon^2_{-1}(X)\}^{1/2}$, and the phase shift $\psi(X)$ by $\psi=\tan^{-1}(\epsilon_{-1}/1+\epsilon_1)$. From (30), it follows that the higher harmonic contributions $m>1$ scale as $\delta\mathcal{V}_m\sim\delta\mathcal{V}_1(1/m^2)$.

B. Mean-field approximation

The exact solutions for the dc and rf fields from the spoke charge are used to obtain "mean-field" solutions for the purposes explained earlier in the outline section. The expression for the dc mean field is computed by replacing the actual spoke profile with a triangular density profile:

$$\hat{n}_0(X)=n_s\left[1-\frac{X-d}{D-d}\right]\ . \tag{42}$$

The effective density n_s is then determined by setting the effective spoke potential resulting from Eq. (42) equal to the exact value $\delta\mathcal{V}_0(\mathcal{D})$ from Eq. (34). Thus the mean dc field, including the hub- and spoke-charge contributions, is given by

$$-\hat{\mathcal{V}}_0(X)=\begin{cases}E_cX-(1/2)\omega_p^2X^2\ , & X<d\\ E_cX-\omega_p^2d\left[X-\dfrac{d}{2}\right]\\ \qquad -\frac{1}{2}\omega_s^2(X-d)^2\left[1-\dfrac{1}{3}\dfrac{X-d}{D-d}\right]\ , & X>d\ ,\end{cases} \tag{43a}$$

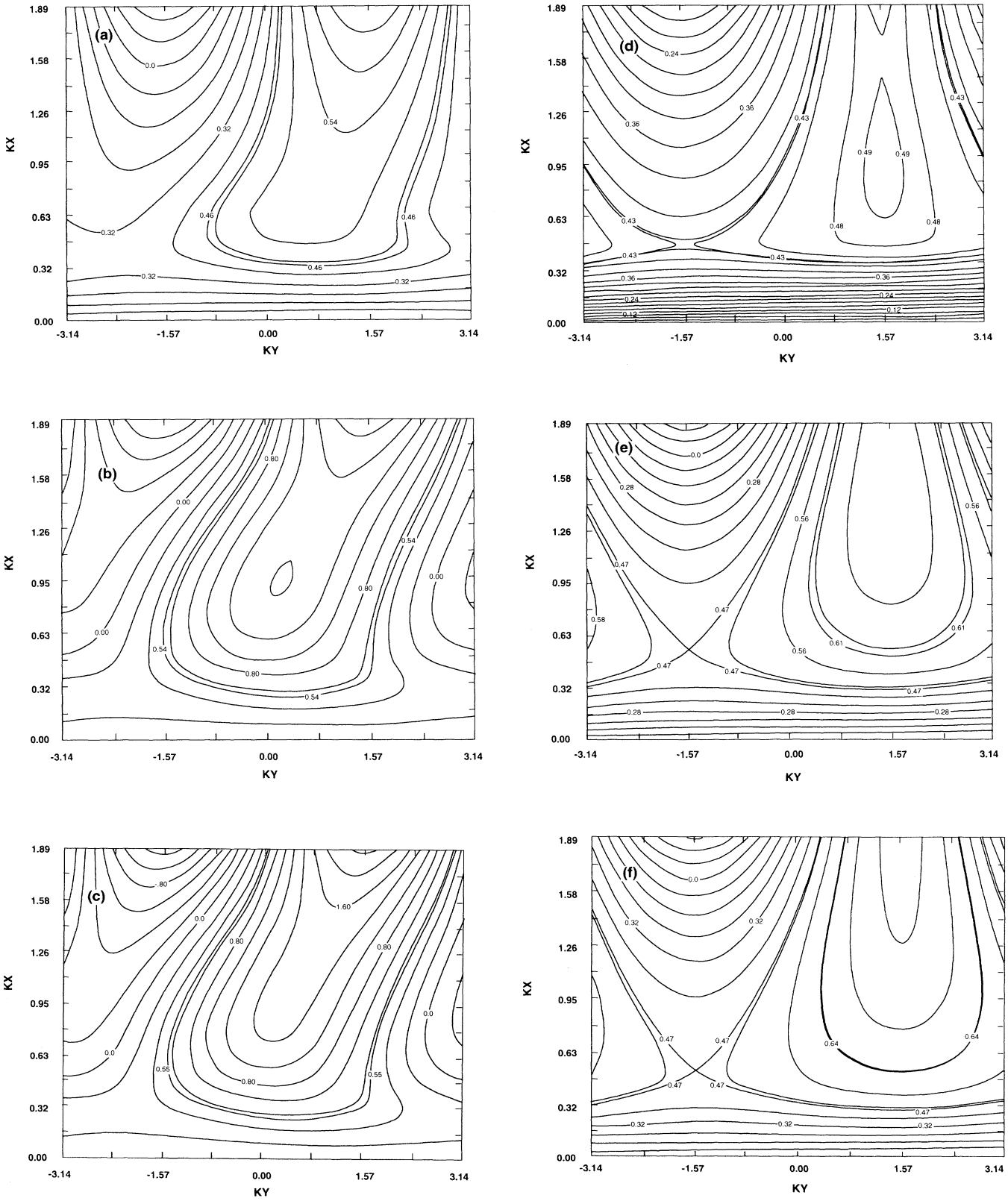

FIG. 4. (a)–(c) Equipotentials from the exact solutions with spoke charge fields, computed at (a) 1.50, (b), 12.75, and (c) 15.25 wavelengths along the interaction space during the run discussed in Figs. 6 and 7. The respective mean-field equipotentials are shown in (d)–(f).

and the mean dc electric field by

$$\hat{E}_0(X)=\begin{cases} E_c-\omega_p^2 X\ , & X>d \\ E_c-\omega_p^2 d-\omega_s^2(X-d)\left[1-\frac{1}{2}\frac{X-d}{D-d}\right]\ , & X<d\ , \end{cases} \tag{43b}$$

where $\omega_p^2=-4\pi n_0$, $\omega_s^2=-4\pi n_s$, and $n_s=-3\delta\mathcal{V}_0(D)/4\pi(D-d)^2$. The cathode field is expressed in terms of ω_p and $v_{\rm dc}$ as

$$E_c=-\frac{V_{\rm dc}}{D}+\omega_p^2 d\left[1-\frac{d}{2D}\right]+\tfrac{1}{3}\omega_s^2 D\left[1-\frac{d}{D}\right]^2 . \tag{44}$$

The sought after approximation $\hat{\mathcal{V}}$ for the total rf field $\mathcal{V}'$, Eq. (39), contains constant $\hat{\Lambda}$ and $\hat{\psi}$:

$$\hat{\mathcal{V}}_1(X,Y)=-\hat{\Lambda}\tilde{V}_1\sinh X\sin(Y+\hat{\psi})\ . \tag{45}$$

Expression (45) preserves the geometric similarity with the vacuum rf profiles and makes the equations analytically tractable. The goal is to select $\hat{\Lambda}$ and $\hat{\psi}$ in order to yield amplitude growth rates and phase slippages that closely approximate those obtained from the exact profiles. The complex growth rate depends on the fast-time, short-scale averaged $\mathbf{J}\cdot\mathbf{E}_1$, where $\mathbf{E}_1$ is the vacuum solution and $\mathbf{J}$ is the spoke current. Since $\mathbf{J}$ is determined from the parapotential GC flow, $\mathbf{J}\propto-\hat{\mathbf{z}}\times\nabla\mathcal{V}/\Omega$, we seek $\hat{\Lambda}$ and $\hat{\psi}$ producing $\mathbf{E}\times\mathbf{B}$ flow as close as possible to the exact solution over one wavelength area. Thus $\hat{\Lambda}$ and $\hat{\psi}$ are obtained by the minimization of

$$I=\int_0^D dX\int_0^{2\pi} dY\{\hat{\mathbf{z}}\times[\nabla\mathcal{V}_1'(X,Y)-\nabla\hat{\mathcal{V}}_1(X,Y;\hat{\Lambda},\hat{\psi})]\}^2\ . \tag{46}$$

The variation of (46) in $\hat{\Lambda}$ and $\hat{\psi}$, performed in Appendix D, yields

$$\hat{\psi}=\tan^{-1}\left[\frac{\langle\epsilon_1\sinh^2X+\epsilon_1'\cosh^2X\rangle}{\langle(1+\epsilon_1)\sinh^2X+(1+\epsilon_{-1}')\cosh^2X\rangle}\right], \tag{47}$$

$$\hat{\Lambda}=\frac{\{\langle\epsilon_1\sinh^2X+\epsilon_1'\cosh^2X\rangle^2+\langle(1+\epsilon_1)\sinh^2X+(1+\epsilon_{-1}')\cosh^2X\rangle^2\}^{1/2}}{\langle\sinh^2X+\cosh^2X\rangle}\ , \tag{48}$$

where we have defined $\epsilon_{\pm1}(X)=\delta\mathcal{V}_{\pm1}(X)/\tilde{V}_1\sinh X$, $\epsilon_{\pm1}'(X)=[(d/dx)\delta\mathcal{V}_{\pm1}(X)]/\tilde{V}_1\cosh X$, and $\langle\ \rangle\equiv\int_0^D dX$. We can appreciate the relation between the exact and mean-field solutions by comparing Figs. 4(a)–4(c) to Figs. 4(d)–4(f). The equipotentials for the total field $\mathcal{V}=\mathcal{V}_0+\mathcal{V}_1'$ from Eqs. (39) and (40) are shown in Figs. 4(a)–4(c) for three different cases. The corresponding mean-field approximations $\mathcal{V}=\mathcal{V}_0+\hat{\mathcal{V}}_1$, with $\hat{\Lambda}$ and $\hat{\psi}$ computed from Eqs. (46) and (47), are shown in Figs. 4(e) and 4(f), respectively.

VI. FLUX CONSERVATION

In the synchronous frame, the amplitudes of the dc and rf components vary slowly with time. Thus, for a moving observer, $\nabla\cdot\mathbf{J}\neq0$, despite the incompressibility. This of course is due to the varying hub density, which is the source of the spoke flow. This slow time variation in the moving frame is connected with the slow spatial variation in the laboratory by the conservation of the total time derivative $(\partial/\partial t)_{\rm syn}=(v_p\partial/\partial y)_{\rm lab}=d/dt$. We therefore transform to the laboratory frame to take advantage of the current conservation imposed by the steady state there. The current density $J(x,y;t)$ above the hub is given by

$$\mathbf{J}(x,y;t)=\int dX\int dY(\mathbf{J}_0+\mathbf{J}_1)\delta(X-x)\delta(Y-y+v_pt)\times[G(Y-\hat{Y}_1(X))-G(Y-\hat{Y}_2(X))]\ , \tag{49}$$

where the term

$$\mathbf{J}_0(X,Y)=n_0(\bar{y}(X))\left[v_p-\frac{1}{\Omega}\frac{d\hat{\mathcal{V}}_0}{dX}\right]\hat{\mathbf{y}} \tag{50}$$

is the contribution from the dc drift, and

$$\mathbf{J}_1(X,Y)=\frac{n_0(\bar{y}(X))}{\Omega}\hat{\mathbf{z}}\times\hat{\mathbf{E}}_1\ ,\qquad \hat{\mathbf{E}}_1(X,Y)=-\nabla\hat{\mathcal{V}}_1(X,Y) \tag{51}$$

results from the rf drift. The δ function transfers from the synchronous frame to the laboratory frame. The step functions G make the density zero outside the spoke boundaries given by the curves $\hat{Y}_{1,2}(X)$. The dc current component is given by the rf period averaging of (49), yielding

$$\langle\mathbf{J}(x,y,t)\rangle\equiv\frac{1}{2\pi}\int_{t-\pi}^{t+\pi}dt'\mathbf{J}(x,y,t)=\frac{1}{2\pi}\int_{\hat{Y}_1}^{\hat{Y}_2}dY'[\mathbf{J}_0(X,Y')+\mathbf{J}_1(X,Y')]\ . \tag{52}$$

Thus the period-averaged current in the laboratory frame at position y and time t equals the wavelength-averaged current in the synchronous frame with its origin at $y=v_pt$.

Taking the dc component of the continuity equation in the laboratory frame, and using the steady-state condi-

tion $\partial/\partial t=0$, yields

$$\nabla\cdot\langle \mathbf{J}\rangle=0 \ . \tag{53}$$

Condition (53) is exact, independent of the adiabatic approximation $\partial/\partial y \ll 1$, and imposes flux conservation along the streamlines in the *laboratory* frame. It follows that the dc current through any cross section between the streamlines is conserved. In particular, choosing the length of the y cross section equal to one wavelength (2π in normalized units), one finds from (28) and (9)

$$I_x(X;y)=2\pi h\langle J_x(X;y)\rangle=I_x(X;t)$$
$$=h\hat{\Lambda}\int_{\hat{Y}_1}^{\hat{Y}_2}dY\frac{\tilde{V}_1}{\Omega}n_0(\bar{y})\sinh X\cos(Y+\hat{\psi}) \ , \tag{54}$$

where $\hat{Y}_1(X)$ and $\hat{Y}_2(X)$ are the two streamlines defining the boundaries of the plasma spoke. The spoke current I_x is invariant along the flow, and equal in both frames of reference. Current conservation implies $I_x(X;y)=I_x(d;y-v_p\tau(X))\equiv I_0(\bar{y}(X))$, where the current I_0 at the spoke base is

$$I_0(\bar{y})=h\hat{\Lambda}n_0(\bar{y})\frac{\tilde{V}_1(\bar{y})}{\Omega}\sinh(d)\int_{\hat{Y}_{10}}^{\hat{Y}_{20}}dY_0\cos(Y_0+\hat{\psi}) \ . \tag{55}$$

It is sufficient to know the current at the base of the spoke at previous times t, or positions y, to determine the current anywhere inside the spoke at later times. This is shown schematically in Fig. 5. The average flight time $\tau(X)$, which is usually much longer than the cyclotron period,

$$\tau(X)=\frac{\int_{\hat{Y}_1}^{\hat{Y}_2}dY\tau_0(X,Y)\cos Y}{\sin Y_2-\sin Y_1} \ , \tag{56}$$

is computed in Appendix B.

The y component I_y of the dc current is also conserved between streamlines. However, since no two full cross sections across the anode-cathode space can be connected with the same streamlines, the total y current flowing along the tube ("circulating current") is not conserved.

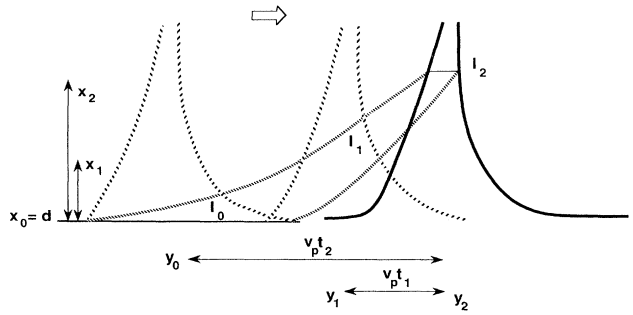

FIG. 5. Sketch of the spoke motion in the synchronous and the laboratory frame, illustrating the effects of flight time and flux conservation.

VII. EVOLUTION OF THE RF SIGNAL

The slow amplitude evolution along the tube for a rf signal of given frequency ω is obtained from the energy balance equation in the laboratory frame. By averaging Maxwell's equations over the fast temporal and spatial scale, one obtains at steady state

$$v_g\frac{\partial\langle W\rangle}{\partial y}=\langle \mathbf{J}\cdot\mathbf{E}_1\rangle \ , \tag{57}$$

where $v_g=\partial\omega/\partial k$ is the group velocity, W is the rf energy density $W=E_1^2/8\pi$, and $\mathbf{J}$ is the *total* current density Eq. (52), including the spoke-charge effects. The equation for the low phase shift is obtained from

$$2v_g\langle W\rangle\frac{\partial\phi}{\partial y}=\langle \mathbf{J}\cdot\tilde{\mathbf{E}}_1\rangle \ , \tag{58}$$

where $\tilde{E}_1(ky)\equiv E_1(ky+\pi/2)$. In complex notation, the right-hand sides of Eqs. (57) and (58) are the real and imaginary parts, respectively, of $\langle \mathbf{J}\cdot\mathcal{E}_1\rangle$, where $\mathcal{E}_1$ is derived from the complex potential $\mathcal{V}_1=V_1(y)e^{i\phi(y)}e^{i(ky-\omega t)}$. The current from the cyclotron rotation $\mathbf{J}_c=n(X,Y)\int d\mathbf{v}_\perp\mathbf{v}_\perp$ is absent from Eqs. (57) and (58). It is shown in Appendix C that the average energy exchange $\langle \mathbf{J}_c\cdot\mathbf{E}_1\rangle$ of a uniform distribution in the cyclotron angle θ is zero for any value of $k\rho$.

We now compute the averages in Eqs. (57) and (58) over the volume of a slice of the tube one wavelength long. The volume on the left-hand side extends over the total cross section ΔS to include the energy stored in the vane structure above the anode ("anode circuit"). Since, on the other hand, energy exchange occurs only in the interaction space, the right-hand side comes from the volume element $\Delta x\Delta y\Delta z$ with $\Delta x=\hat{D}$, $\Delta y=\lambda=2\pi$ and $\Delta z=h$, the axial length of the tube. Equation (57) then yields

$$\lambda\frac{\partial}{\partial y}v_g\int\int_{\Delta S}d^2\mathbf{r}\,W=\int_0^{\hat{D}}\int_0^{\lambda}\int_0^{h}d^3\mathbf{r}\,\mathbf{J}\cdot\mathbf{E}_1 \ . \tag{59}$$

Expression (59) amounts to averaging over the volume of a "window" one wavelength long, centered around y, the traveled distance along the tube. Truncating the X integration at $\hat{D}<D$ takes into account that the average GC position at the moment of impact lies below the anode; neglecting rf drift corrections, $\hat{D}=D-\rho$. The left-hand side, the power flow along the tube, is by definition related to the interaction impedance $\mathcal{Z}_i$ by

$$v_g\int\int_{\Delta S}d^2\mathbf{r}\,W=\frac{V_1^2}{2\mathcal{Z}_i} \ . \tag{60}$$

Substituting Eq. (60) inside Eq. (59) yields the growth-rate equation for the amplitude V_1:

$$\frac{\partial}{\partial y}\frac{V_1^2}{2\mathcal{Z}_i}=\frac{h}{\lambda}\int_0^{\hat{D}}dx\int_0^{\lambda}dy\,\mathbf{J}\cdot\mathbf{E}_1 \ . \tag{61}$$

The equation for the slow phase ϕ, from the averaging of the right-hand side of Eq. (58), is

$$2\frac{V_1^2}{2Z_i}\frac{\partial\phi}{\partial y}=\frac{h}{\lambda}\int_0^{\hat{D}}dx\int_0^{\lambda}dy\,\mathbf{J}\cdot\tilde{\mathbf{E}}_1\ . \tag{62}$$

Expression (52) for the total crurent is employed to evaluate the dot products in the rhs of Eqs. (61) and (62). To that purpose, we first express the mean rf field inside Eq. (51) for $\mathbf{J}_1$ in terms of the vacuum cavity (unperturbed) rf fields. From $\hat{\mathbf{E}}_1(X,Y)=-\nabla\hat{V}_1(X,Y)$ it follows that

$$\hat{\mathbf{E}}_1=\cos(\hat{\psi})\mathbf{E}_1+\sin(\hat{\psi})\tilde{\mathbf{E}}_1 \tag{63}$$

where the in- and out-of-phase vacuum fields are given by

$$\mathbf{E}_1=\begin{bmatrix}\tilde{V}_1\cosh X\sin Y\\ \tilde{V}_1\sinh X\cos Y\end{bmatrix},\qquad \tilde{\mathbf{E}}_1=\begin{bmatrix}\tilde{V}_1\cosh X\cos Y\\ -\tilde{V}_1\sinh X\sin Y\end{bmatrix}. \tag{64}$$

Combining Eqs. (51), (63), and (64), one obtains

$$\begin{aligned}\hat{\mathbf{J}}\cdot\mathbf{E}_1&=\frac{n(X)}{\Omega}[\hat{\mathbf{E}}_0\cdot\mathbf{E}_1+\sin(\hat{\psi})\ (\hat{\mathbf{z}}\times\tilde{\mathbf{E}}_1)\cdot\mathbf{E}_1]\\&=\frac{n(X)}{\Omega}[\hat{E}_0E_{1y}+\sin(\hat{\psi})\ (-\tilde{E}_{y1}E_{x1}+\tilde{E}_{x1}E_{y1})]\\&=\frac{n(X)\tilde{V}_1}{\Omega}[\hat{E}_0(X)\sinh X\cos Y+\tfrac{1}{2}\hat{\Lambda}\sin(\hat{\psi})\ \tilde{V}_1\sinh 2X]\ ,\end{aligned} \tag{65}$$

$$\begin{aligned}\hat{\mathbf{J}}\cdot\tilde{\mathbf{E}}_1&=\frac{n(X)}{\Omega}[\hat{\mathbf{E}}_0\cdot\tilde{\mathbf{E}}_1+\cos(\hat{\psi})\ (\hat{\mathbf{z}}\times\mathbf{E}_1)\cdot\tilde{\mathbf{E}}_1]\\&=\frac{n(X)}{\Omega}[\hat{E}_0\tilde{E}_{1y}+\cos(\hat{\psi})\ (-E_{y1}\tilde{E}_{x1}+E_{x1}\tilde{E}_{y1})]\\&=-\frac{n(X)\tilde{V}_1}{\Omega}[\hat{E}_0(X)\sinh X\sin Y+\tfrac{1}{2}\hat{\Lambda}\cos(\hat{\psi})\ \tilde{V}_1\sinh 2X]\ .\end{aligned} \tag{66}$$

Inserting expressions (65) and (66) inside the rhs of Eqs. (61) and (62), respectively, the amplitude growth and the phase slippage equations are recast in the form

$$\begin{aligned}\frac{dV_1}{dy}=\frac{hZ_i}{2\pi V_1}\Bigg[&\int_d^{\hat{D}}dX\,\hat{E}_0(X;y)n_0(\bar{Y})\frac{V_1}{\Omega\sinh D}\sinh(X)\int_{\hat{Y}_1}^{\hat{Y}_2}dY\cos(Y+\hat{\psi})\\&+\hat{\Lambda}\sin(\hat{\psi})\int_d^{\hat{D}}dX\,n_0(\bar{y})\frac{V_1^2}{\Omega\sinh^2 D}\sinh X\cosh(X)\int_{\hat{Y}_1}^{\hat{Y}_2}dY\Bigg]\ ,\end{aligned} \tag{67a}$$

$$\begin{aligned}\frac{d\phi}{dy}=-\frac{hZ_i}{2\pi V_1^2}\Bigg[&\int_d^{\hat{D}}dX\,\hat{E}_0(X;y)n_0(\bar{y})\frac{V_1}{\Omega\sinh D}\sinh(X)\int_{\hat{Y}_1}^{\hat{Y}_2}dY\sin(Y+\hat{\psi})\\&+\hat{\Lambda}\cos(\hat{\psi})\int_d^{\hat{D}}dX\,n_0(\bar{y})\frac{V_1^2}{\Omega\sinh^2 D}\sinh X\cosh(X)\int_{\hat{Y}_1}^{\hat{Y}_2}dY\Bigg]\ .\end{aligned} \tag{67b}$$

The main nonlinearities in Eqs. (67) are hidden in the spoke boundaries $\hat{Y}_{1,2}(X)$, which are nonlinear functions of V_1 according to the Hamiltonian flow (9), and in the delay time of the retarded position $\bar{y}$.

The evolution equations can be put in a more instructive form by neglecting the terms $O(V_1^2)$ in the rhs of (67b), since usually $kV_1/E_0\ll 1$. Utilizing expression (54) for the current $I_x(X;y)$, Eqs. (67) are reformulated as

$$\frac{dV_1}{dy}=\frac{Z_i}{2\pi V_1}\frac{1}{\hat{\Lambda}}\int_d^{\hat{D}}dX\,\hat{E}_0(X;y)I_x(X;y)+O(V_1^2)\ , \tag{68a}$$

$$\frac{d\phi}{dy}=\frac{Z_i}{2\pi V_1^2}\frac{1}{\hat{\Lambda}}\int_d^{\hat{D}}dX\,\hat{E}_0(X;y)\tilde{I}_x(X;y)+O(V_1^2)\ . \tag{68b}$$

Thus the lowest-order power gain is determined by the streamlines reaching the anode, i.e., the in-phase ("resistive") current I_x, as one would expect from a simple circuit model. The phase slippage is related to the out-of-phase ("reactive") current $\tilde{I}_x$, defined by the substitution $\cos(Y+\hat{\psi})\rightarrow\cos(Y+\hat{\psi}+\pi/2)=-\sin(Y+\hat{\psi})$ inside Eq. (54). Note that current conservation, Eq. (55), allows the substitution of $I_x(X;y)$ with the current at the spoke base

in the retarded location $I_0(\bar{y})$; conservation does not apply to $\tilde{I}_x$. In perfect synchronism we have only resistive current with zero reactive contribution, $\tilde{I}_x=0$ and $d\phi/dy=0$. Far from synchronism we may have pure reactive current $\tilde{I}_x$, even when the anode current is cutoff $I_x=0$ and $dV/dy=0$.

VIII. DISCUSSION OF THE DIELECTRIC EFFECTS

The importance of the spoke-charge effects can be appreciated by comparing the growth rate, Eqs. (67a) and (67b), with the growth rate in the absence of spoke self-fields. To do so, we must first express Eqs. (67) in terms of the "unperturbed" spoke boundaries. The spoke boundaries in the mean-field potential are shifted relative to their location in the vacuum fields by $-\hat{\psi}$. If one defines $\langle \cos Y \rangle$ and $\langle \sin Y \rangle$ as the averages over the unperturbed spoke boundaries, then the self-consistent spoke boundaries yield

$$\begin{aligned}\int_{Y_1-\hat{\psi}}^{Y_2-\hat{\psi}} dY \cos Y &= \cos\hat{\psi}\langle \cos Y \rangle + \sin\hat{\psi}\langle \sin Y \rangle \ , \\ \int_{Y_1-\hat{\psi}}^{Y_2-\hat{\psi}} dY \sin Y &= \cos\hat{\psi}\langle \sin Y \rangle - \sin\hat{\psi}\langle \cos Y \rangle \ .\end{aligned} \tag{69}$$

Combining (67) and (69) yields the final result

$$\begin{aligned}\frac{dV_1}{dy} = \frac{h\mathcal{Z}_i}{2\pi V_1} \Bigg[& \cos(\hat{\psi}) \int_d^D dX\, \hat{E}_0(X;y) n_0(\bar{y}) \frac{V_1}{\Omega \sinh D} \sinh(X) \int_{Y_1}^{Y_2} dY \cos Y \\ & + \sin(\hat{\psi}) \int_d^D dX\, \hat{E}_0(X;y) n_0(\bar{y}) \frac{V_1}{\Omega \sinh D} \sinh(X) \int_{Y_1}^{Y_2} dY \sin Y \\ & + \tfrac{1}{2}\hat{\Lambda} \sin(\hat{\psi}) \int_D^D dX\, n_0(\bar{y}) \frac{V_1^2}{\Omega \sinh^2 D} \sinh(2X) \int_{Y_1}^{Y_2} dY \Bigg] \ ,\end{aligned} \tag{70a}$$

$$\begin{aligned}\frac{d\phi}{dy} = -\frac{h\mathcal{Z}_i}{2\pi V_1^2} \Bigg[& \cos(\hat{\psi}) \int_d^D dX\, \hat{E}_0(X;y) n_0(\bar{y}) \frac{V_1}{\Omega \sinh D} \sinh(X) \int_{Y_1}^{Y_2} dY \sin Y \\ & - \sin(\hat{\psi}) \int_d^D dX\, \hat{E}_0(X;y) n_0(\bar{y}) \frac{V_1}{\Omega \sinh D} \sinh(X) \int_{Y_1}^{Y_2} dY \cos Y \\ & + \tfrac{1}{2}\hat{\Lambda} \cos(\hat{\psi}) \int_d^D dX\, n_0(\bar{y}) \frac{V_1^2}{\Omega \sinh^2 D} \sinh(2X) \int_{Y_1}^{Y_2} dY \Bigg] \ .\end{aligned} \tag{70b}$$

The earlier results [13,14], neglecting the spoke-charge effects, are now recovered from (70) at the limit $\hat{\Lambda}=1$ and $\hat{\psi}=0$:

$$\begin{aligned}\frac{dV_1}{dy} = \frac{h\mathcal{Z}_i}{2\pi V_1} & \int_d^{\hat{D}} dX\, E_0(X;y) n_0(\bar{y}) \\ & \times \frac{V_1}{\Omega} \sinh(X) \int_{Y_1}^{Y_2} dY \cos Y \ ,\end{aligned} \tag{71a}$$

$$\begin{aligned}\frac{d\phi}{dy} = -\frac{h\mathcal{Z}_i}{2\pi V_1^2} \Bigg[& \int_d^{\hat{D}} dX\, E_0(X;y) n_0(\bar{y}) \\ & \times \frac{V_1}{\Omega} \sinh(X) \int_{Y_1}^{Y_2} dY \sin Y \\ & + \tfrac{1}{2} \int_d^{\hat{D}} dX\, n_0(\bar{y}) \frac{V_1^2}{\Omega} \sinh(2X) \int_{Y_1}^{Y_2} dY \Bigg] \ .\end{aligned} \tag{71b}$$

The self-field effects of the spoke now become transparent by first observing that $\gamma \equiv (1/V_1) dV_1/dy$ and $\kappa \equiv d\phi/dy$ are the real and imaginary parts, respectively, of the complex growth rate

$$\Gamma \equiv \gamma + i\kappa \ . \tag{72}$$

A comparison between Eqs. (70) and (71) shows that in the low space-charge-density limit, when $\Lambda = 1 + O(\epsilon)$, $\psi = O(\epsilon)$, $|\epsilon| \ll 1$, one has

$$\begin{aligned}\gamma &= \cos(\hat{\psi})\ \gamma_0 - \sin(\hat{\psi})\ \kappa_0 + O(\epsilon^2) \ , \\ \kappa &= \sin(\hat{\psi})\ \gamma_0 + \cos(\hat{\psi})\ \kappa_0 + O(\epsilon^2) \ ,\end{aligned} \tag{73}$$

where the subscript $(_0)$ denotes absence of spoke fields. Thus, the lowest-order dielectric effects manifest as a rotation of the complex growth rate by the mean-field phase shift $\hat{\psi}$:

$$\Gamma = e^{i\hat{\psi}} \Gamma_0 \ . \tag{74}$$

The total power $P_{\text{out}} - P_{\text{in}}$ transfered to the wave over the tube length is, using $J_x = I_x/2\pi h$,

$$\begin{aligned}\int\int_{\text{vol}} \int d^3\mathbf{r}\, \mathbf{J}\cdot\mathbf{E}_1 = \frac{1}{2\pi} & \int_0^L dy \frac{1}{\hat{\Lambda}} \int_d^{\hat{D}} dX\, I_x(X;y) \\ & \times \hat{E}_0(X;y) \ ,\end{aligned} \tag{75}$$

where L is the interaction space length. Exchanging the order of integration in Eq. (75), letting $E_0(X;y) \simeq E_0(X)$

(small variation of E_0 over the interaction space), and observing that at steady state the total current $\mathbf{I}_x(X)\equiv(1/2\pi)\int_0^L dy\, I_x(X;y)$ through any plane parallel to the cathode is constant and equal to the anode current $\mathbf{I}_a$, one obtains an upper limit for the efficiency $\eta\equiv(P_{\rm out}-P_{\rm in})/\mathbf{I}_a V_{\rm dc}$,

$$\eta\le\frac{\int_d^{\hat{D}} dX\, E_0(X)\int_0^L dy\,\hat{\Lambda}^{-1}I_x(X;y)}{\mathbf{I}_a V_{\rm dc}}$$

$$\simeq\left[\frac{1}{\hat{\Lambda}}\right]\left[1-\frac{d+\rho}{D}\right]\frac{1-\dfrac{d}{2D}\dfrac{E_c}{E_{\rm dc}}}{1-\dfrac{d}{2D}}\ . \tag{76}$$

In Eq. (76), $E_{\rm dc}=-V_{\rm dc}/D$, the total dc anode current is given by

$$\mathbf{I}_a=\frac{1}{2\pi}\int_0^L dy\, I_a(y)\ , \tag{77}$$

and $\langle 1/\hat{\Lambda}\rangle\equiv(1/L)\int_0^L dy/\hat{\Lambda}$. The equals sign in the efficiency Eq. (76) applies in the case of magnetrons where the spokes and the rf amplitudes do not vary along y.

The effect of the space-charge electrostatic energy on the tube interaction impedance is now briefly addressed. By definition, the interaction impedance relates the total power flux $\mathcal{P}$ along the tube to the rf voltage at the anode,

$$\frac{V_1^2}{2Z_i}=\mathcal{P}=\mathcal{P}_{\rm cir}(V_1)+\mathcal{P}_{\rm rf}(V_1)\ . \tag{78}$$

The power flow in the "anode circuit" $\mathcal{P}_{\rm cir}$, the structure supporting the slow wave, depends mainly on the circuit characteristics and is not changed considerably by the charge circulating in the anode-cathode gap. The latter affects mainly the power flow in the anode-cathode gap, given by

$$\mathcal{P}_{\rm rf}=v_g h\int_0^D dX\int_0^{2\pi} dY\left[\frac{1}{8\pi}|\mathbf{E}_1|^2+\tfrac{1}{2}n\mathcal{V}_1\right]\ , \tag{79}$$

where the first term represents the energy stored in the vacuum fields and the second is the potential energy of the space charge in the rf field. Thus, the ratio of the cold cavity interaction impedance to the self-consistent value is given by

$$\frac{Z_i}{Z_i^0}=\frac{1+\dfrac{\mathcal{P}_{\rm rf}^0}{\mathcal{P}_{\rm cir}}}{1+\dfrac{\mathcal{P}_{\rm rf}}{\mathcal{P}_{\rm cir}}}\ . \tag{80}$$

Given that

$$\frac{\mathcal{P}_{\rm rf}^0}{\mathcal{P}_{\rm rf}}=1+\frac{\int_0^D dX\int_0^{2\pi} dY\frac{1}{8\pi}|\mathbf{E}_1|^2}{\int_0^D dX\int_0^{2\pi} dY\frac{1}{2}n\mathcal{V}_1}\ , \tag{81}$$

and that $\mathcal{P}_{\rm rf}^0$ is usually much smaller than the circuit power flux $\mathcal{P}_{\rm cir}$, Eqs. (80) and (81) yield for $\mathcal{P}_{\rm rf}^0/\mathcal{P}_{\rm cir}\ll 1$

$$Z_i\simeq Z_i^0\left[1-\frac{\int_0^D dX\int_0^{2\pi} dY\frac{1}{2}n\mathcal{V}_1}{\int_0^D dX\int_0^{2\pi} dY\frac{1}{8\pi}|\mathbf{E}_1|^2}\frac{\mathcal{P}_{\rm rf}^0}{\mathcal{P}_{\rm cir}}\right]\ . \tag{82}$$

For the simulated case, the ratio $\mathcal{P}_{\rm rf}^0/\mathcal{P}_{\rm cir}\simeq\frac{1}{25}$ over the operation frequency band, thus the impedance modification remains small when the spoke self-energies are of the same order as the energy stored in the vacuum field of the anode-cathode space.

IX. NUMERICAL SOLUTIONS AND DISCUSSION

Differential equations (20), (67a), and (67b) for n_0, V_1, and ϕ, supplemented by the dielectric response Eq. (40), the mean-field parameters Eqs. (47) and (48), and the auxilliary equations (21), (22), (55), and (56) for the secondary emission, the impact energy, the spoke current and the flight time, respectively, consistute a closed set. A numerical algorithm has been constructed for the integration of the above equations. The exact spoke fields, obtained from the spoke boundaries at a given simulation step, are used to compute the amplitude growth rate and phase shift. The mean-field approximation is then employed to update the spoke boundaries for the next step. Earlier numerical results, ignoring spoke-charge effects, have appeared in previous reports [13,14]. The physical issues for CFA operation have been discussed there in some detail. Here we focus on the effects caused by the inclusion of spoke charge. The evolution of the hub density, rf amplitude, and phase, during a typical pass through the tube, is shown in Fig. 6. The dashed lines show results for the same pass when spoke-charge effects are turned off. The normalized cathode field $E_c/E_{\rm dc}$, the spoke current at the top of the spoke I_a (normalized to the total anode current), and the quantity $\delta^*=\delta-1$ for the same pass appear in Fig. 7. The tube parameters are

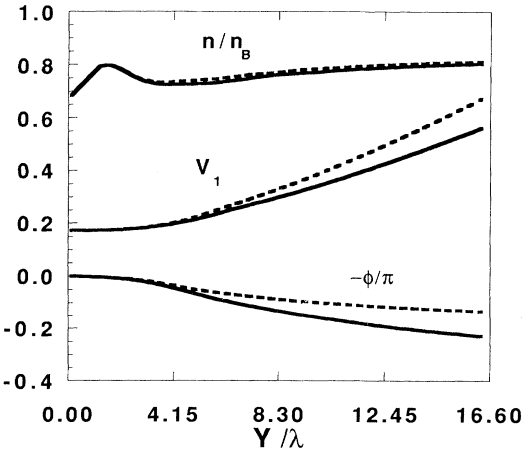

FIG. 6. Evolution of the normalized rf amplitude, rf phase and hub density during a single pass for $V_{\rm dc}=3.991$, $P_{\rm rf}(in)=0.263$, $B_0=2.29$, and midband frequency. Dashed lines show results without spoke fields.

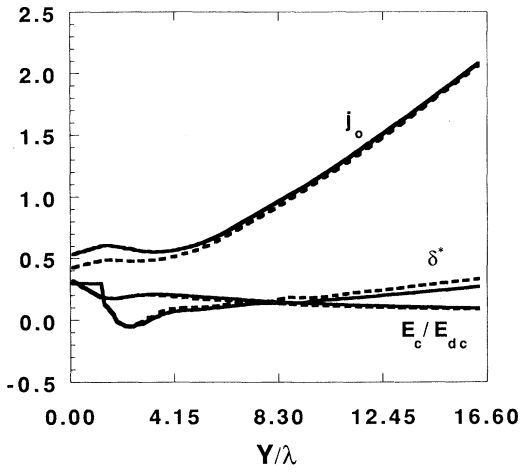

FIG. 7. Same as in Fig. 6 for the cathode field, the secondary emission margin $\delta^*=\delta-1$ and the spoke current j_0 (normalized to $\frac{1}{10}$ of the total current, $j_0=10I/I_0$).

$V_{dc}=3.991$, $B=2.29$, $P_{rf}(\text{in})=0.263$ and midband frequency f_0, corresponding to an interaction length of $16\frac{1}{4}$ wavelengths. The hub height was fixed at $d=d_B$ throughout the parameter range, where the Brillouin height $d_B=D[1-(1-2V_{dc}/D^2\Omega^2)^{1/2}]$.

The importance of the spoke charge can be inferred from the results in Fig. 8. Shown are the dielectric responses $\langle\epsilon_1\rangle$ and $\langle\epsilon_{-1}\rangle$, averaged over the anode-cathode gap, against the traveled distance along the tube. Also plotted is the ratio of W/W_{rf}, where $W=W_{rf}+W_{es}$ is the total energy in the gap (per wavelength), W_{es} is the spoke charge electrostatic energy,

$$W_{es}=\tfrac{1}{2}\int_0^D dX\int_{\hat{Y}_1}^{\hat{Y}_2} dY\,\hat{\mathcal{V}}_1(X,Y)n_0(\bar{y})\ , \tag{83}$$

and W_{rf} is the vacuum rf energy,

$$W_{rf}=\frac{1}{8\pi}\int_0^D dX\int_{\hat{Y}_1}^{\hat{Y}_2} dY\,\mathbf{E}_1^2\ . \tag{84}$$

An interesting feature is that dielectric effects peak early during a tube pass, at low rf power and spoke current, and then decrease monotonically, despite the increase in the spoke current. The spoke charge responsible for the dielectric effects builds up within the time interval that a rising spoke reaches the anode. The spoke charge and the related self-field remain nearly constant thereafter, since the hub density feeding the spoke changes little over the rest of the interaction space. However, the current keeps increasing, because the flow *velocity* $u\sim V_1$, Eq. (13), increases as V_1 grows. After the fully developed spoke has formed, the rf wave energy, proportional to V_1^2, grows much faster than the electrostatic spoke energy, proportional to V_1, and the dielectric effects start decreasing.

The evolution of the amplitude factor $\hat{\Lambda}$ and the phase shift $\hat{\psi}$ are shown in Fig. 9. When $\hat{\Lambda}>1$, the mean-field amplitude exceeds the vacuum value and tends to enhance the spoke current, while the phase shift $\hat{\psi}$ pushes the streamlines out of phase relative to the wave phase at the anode. Thus spoke-charge effects generally tend to increase the local field strength and current flow and at the same time pull the current phase out of synchronism from the wave phase. From a comparison with Fig. 8, it is obvious that the mean amplitude $\hat{\Lambda}V_1$ is less than the average amplitude $\bar{V}_1\equiv V_1\sqrt{1+W_{es}/W_{rf}}$ defined from the total energy in the anode-cathode gap. The ratio of the growth rate γ, Eq. (70), to the growth rate without spoke-charge effects, Eq. (71a), also plotted in Fig. 9, demonstrates the combined effect of $\hat{\Lambda}$ and $\hat{\psi}$.

To obtain the time-averaged, near-steady-state operation quantities, such as the average total current at the anode, the average output rf voltage and the average phase slippage from the nominal frequency, the code runs

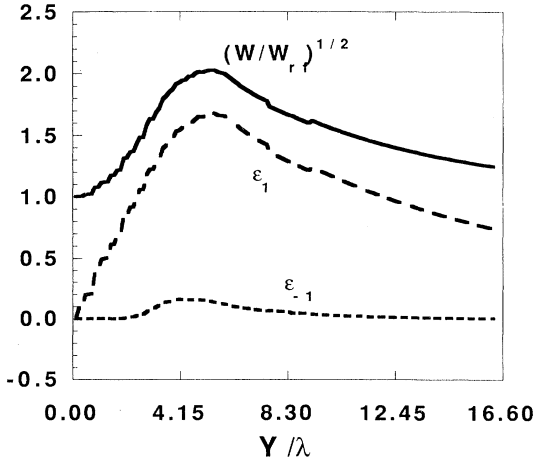

FIG. 8. Dielectric effects along the same tube pass as in Fig. 6. Plotted are the in-phase and out-of-phase dielectric responses $\langle\epsilon_{\pm1}\rangle$ averaged over the anode-cathode gap, and the ratio of the total gap energy to the vacuum rf energy.

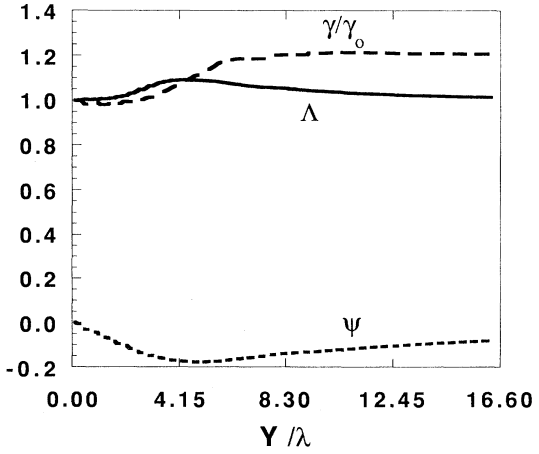

FIG. 9. Plot of the mean field factor $\hat{\Lambda}$, the mean phase shift $\hat{\psi}$, and the ratio γ/γ_0, where γ_0 is the growth rate without dielectric effects.

over many tube passes. The debunching of the spoke in the drift space of the tube is modeled by reshaping the charge distribution of the exiting spoke into a trapezoidal profile, 2π wide at the base, π wide at the top and centered at $Y=0$. The total charge is conserved in this intuitive treatment by adjusting the spoke-charge density, but the circulating current is not. The hub-charge recirculation in the drift space is modeled by integrating the density Eq. (20) setting the current at the top of the hub $I_0=0$. The impact energy for the secondary emission is determined by the self-field of the "collapsed" spoke. After reentering at the input, the spoke remnants are consistently treated, as part of the total space charge. They contribute to the charge of the new, rising spoke and in the anode current. The results, plotted in Fig. 10, show the relative rf amplitude $V_{\rm rf}({\rm out})/V_{\rm dc}$, the phase pushing $\Delta\phi=\phi({\rm out})$, and the hub density n_0 [in units of the Brillouin density $n_B=(m_e/4\pi e^2)\Omega^2$] at the output versus the pass number. The same quantities without dielectric effects appear as dashed lines for comparison. The total anode current $\mathbf{I}_a$ during each pass, given by (77), and the total current at the top of the plasma hub $\mathbf{I}_0$ (given by a similar expression), are shown in Fig. 11 with and without dielectric effects. The difference between the anode and the cathode current is due to the finite time of flight τ. The charge emitted from the cathode near the end of each pass $T-\tau<t<T$, $T=L/v_p$ being the tube transit time, reaches the anode only after the spoke reenters at the input (anode current at the drift space is negligible). In the previous code version, which neglected spoke feedback, this current is unaccounted for at the anode. With the inclusion of the spoke feedback, the disparity between the anode-cathode current is reduced, but the current conservation at steady state $\mathbf{I}_a=\mathbf{I}_0$ is still not satisfied. The reason is the intuitive way of handling the spoke collapse in the drift space, which preserves

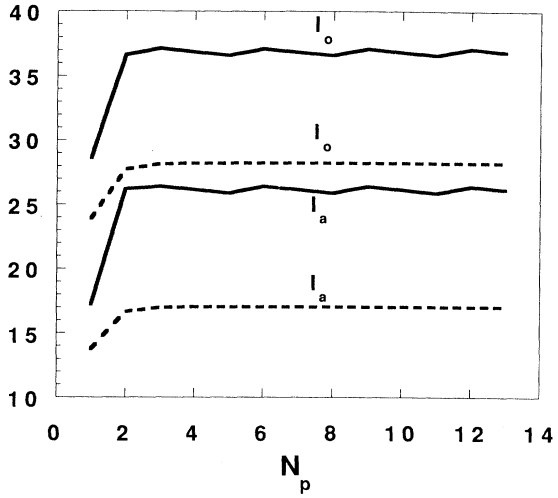

FIG. 11. Same as in Fig. 10 for the total current at the anode $\mathbf{I}_a$ and the top of the hub $\mathbf{I}_0$.

charge but not current (current conservation has been achieved by recycling the spokes unchanged, but this leads to a magnetronlike situation and does not apply to CFA's).

A convergence to a quasisteady state, characterized by small pass-to-pass fluctuations, has been observed over a wide range of operation voltages, frequencies, and secondary-emission coefficients. The existence of the steady state is independent of the initial startup density. The solid line in Fig. 12 shows the characteristic *V-I* curve (dc current $\mathbf{I}_0$ against $V_{\rm dc}$), obtained from the final steady state of multipass simulations, at midband operation frequency, given magnetic field $B=2.29$ and rf input

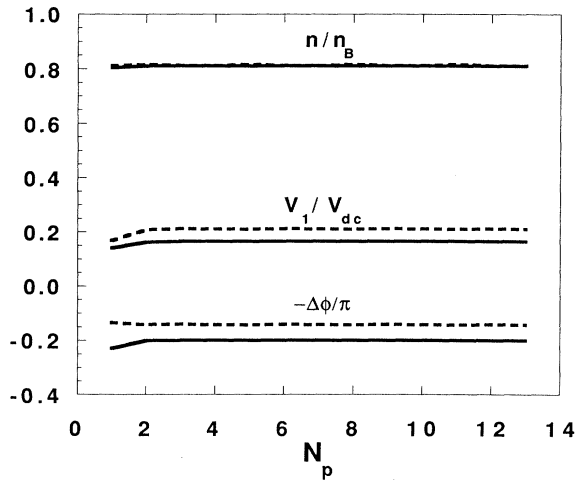

FIG. 10. CFA parameters at the output vs pass number. Shown are the normalized rf amplitude, rf phase, and hub density. Solid lines are results without spoke charge effects. The operation parameters are $V_{\rm dc}=3.991$, $P_{\rm rf}({\rm in})=0.263$, and $B=2.29$ at midband frequency.

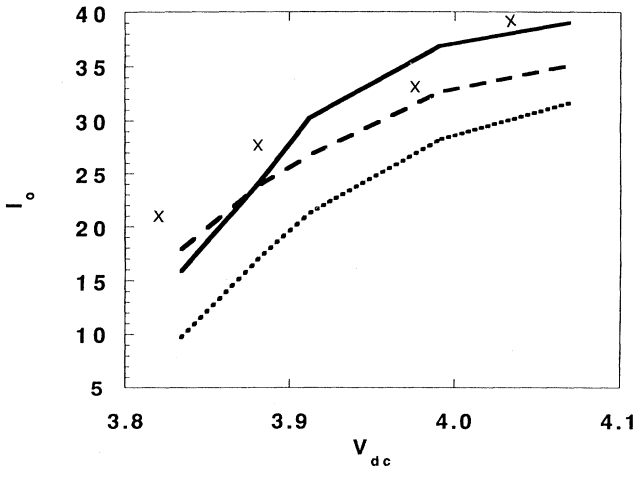

FIG. 12. Comparison of steady-state *V-I* curves (nondimensional units) at midband frequency. Solid line shows the full self-consistent spoke treatment. The dotted line shows results without spoke charge effects. The dashed line includes spoke charge effects in the interaction space but no spoke reentry. Experimental points are marked by ×'s.

power $P_{rf}=0.263$. For comparison, the dotted line shows results without dielectric effects. The dashed line includes dielectric effects in the interaction space but neglects spoke reentry. Figure 13 shows the rf output power corresponding to the results in Fig. 12. Finally, the phase pushing at the output from the nominal vacuum dispersion is shown in Fig. 14. Good agreement with the experimental data marked by ×'s is achieved. According to these results, the spoke self-fields increase considerably both the rf output power and the dc current. The current increase reflects in part the increase in the average rf field strength, caused by the superposition of the 90° out-of-phase spoke rf field. Equally important is the contribution from the spoke-charge reentrance in the input. It has been shown numerically that spoke recirculation increases the output power and anode current even at 180° out-of-phase reentry. The general streamline topology is always such that most of the reentering spoke charge will eventually be recycled towards the anode, resulting in a net current increase and power gain. The agreement with the experimentally observed behavior and the reduction in computation time are major features of the GC model. Note that the per-pass computer CPU time is ~10 sec for a CRAY-2 computer, three orders of magnitude less than particle codes [18,19].

Space-charge recirculation establishes a feedback mechanism between the input and the output that plays a crucial role in the tube noise. It has been already shown [15] that recycling of the hub charge alone may lead to chaotic oscillations in the output when the secondary-emission coefficient exceeds certain thresholds. The input-output coupling via the spoke recirculation constitutes an even stronger feedback mechanism, which will be examined in a separate study. Our preliminary observations show that the output fluctuations over many tube passes depend on (a) the spoke reentry phase relative to the input signal and (b) the degree of spoke "debunching" in the drift space. The rms noise maximizes for in-phase reentry with no spoke debunching. Noise levels and their sensitivity to the reentry phase subside with increased spoke collapse in the drift space. The examination of the rms fluctuations *along* the tube reveals that the noise level builds up within the first one-third of the interaction space, and remains constant or even decreases for the rest of the interaction length. Thus the recycling of the spoke remnants combined with the new spoke formation accounts for most of the overall intrinsic noise in the tube.

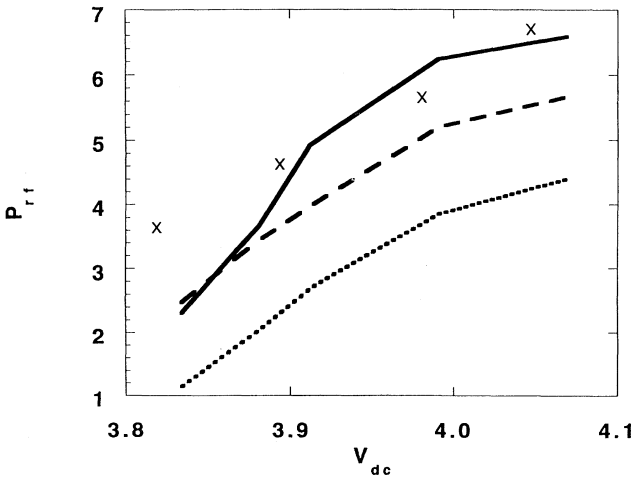

FIG. 13. Same notation as in Fig. 12 for the rf output power vs V_{dc} for fixed input power and midband frequency.

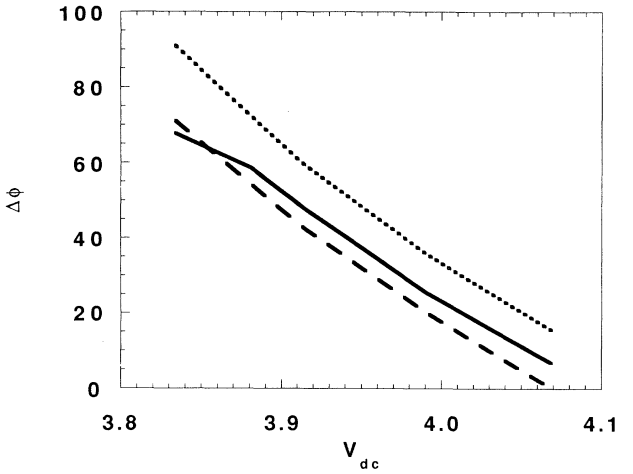

FIG. 14. Same as in Fig. 12 for the phase pushing $\Delta\phi$ from the nominal (vacuum) dispersion at the output.

ACKNOWLEDGMENTS

The author would like to thank Dr. David Chernin, Dr. Y. Y. Lau, Dr. Norm Dionne, Dr. Hunter McDowel, Dr. Rodney Vaughan, and Dr. Adam Drobot for many useful and motivating discussions. This work is supported by the Naval Research Laboratory Contract No. N00014-89-C-2480.

APPENDIX A: IMPACT ENERGY

Secondaries are born with energies of a few eV, much smaller than the dc drift velocities, of the order of hundreds of eV. For simplicity, the impact energy is evaluated, assuming that the electron was originally emitted with zero energy in the stationary (laboratory) frame. The orbit in the crossed electric and magnetic fields of Eq. (5), including the effects of the charged hub, is a deformed epitrohoid: an elliptic orbit around a guiding-center drifting with velocity

$$v_c=\frac{eE_c}{m\Omega}\frac{1}{1-\dfrac{\omega_p^2}{\Omega^2}} . \tag{A1}$$

Switching to dimensionless variables, one has $v_c=\rho_c\Omega$, where $\rho_c=(E_c/\Omega^2)/(1-\omega_p^2/\Omega^2)$. In the frame moving with the cathode drift v_c, the orbit becomes an ellipse:

$$(x-\rho_c)^2+\left[1-\frac{\omega_p^2}{\Omega^2}\right]y^2=\rho_c^2 , \tag{A2}$$

centered around a stationary guiding center, located at $X_c=\rho_c$ and $Y_c=y_0$. When the hub height equals the Brillouin height d_B, it can be shown, using Eq. (7) for E_c, that $\rho_c \to d_B(1-d_B/2D)$, independent of the hub density.

Particles born with $\pi/2 < Y < 3\pi/2$ will be driven back towards the cathode by the rf field and will strike again within a time interval less than a cyclotron period. The impact energy will be evaluated first with no space charge, $\omega_p=0$, and the result will be generalized for finite ω_p. The downward kick received by the electrons guiding center within time $\tau \simeq 2\pi/\Omega$, is, using Eq. (12), $\delta X = u_x(X=\rho, Y)\tau = (V_1/\Omega)\tau \sinh\rho \cos Y'$. Here $Y'=Y-\omega' t$, where $\omega'=\omega-kv_c \neq 0$, since v_c is in general less than v_p. Because $\omega' < \omega < \Omega$, Y' does not change much over a cyclotron period and is taken as constant during the kick. If θ_2 is the impact angle relative to the cathode surface, one has

$$\rho_c(1-\cos\theta_2)=\delta X \ , \tag{A3}$$

$$\rho_c[1-\cos(\theta_2-\Omega\tau)]=0 \ , \tag{A4}$$

where $\rho_c=E_c/\Omega^2$. Because of the smallness of δX compared to ρ_c, θ_2 is $\ll 1$ and one obtains

$$\theta_2 \simeq 2\sin\frac{\theta_2}{2}=\left[\frac{2\delta X}{\rho_c}\right]^{1/2} \tag{A5}$$

from Eq. (A3), and

$$\tau=\frac{1}{\Omega}\left[2\pi-\sin^{-1}\left[\frac{2\delta X}{\rho_c}\right]^{1/2}\right] \tag{A6}$$

from Eq. (A4). The impact velocities in the moving frame are the superposition of the cyclotron motion and the rf drift. Subtracting v_c to go back to the stationary frame yields

$$v_x^i=v_c\sin\theta_2+\frac{\tilde{V}_1}{\Omega}\sinh\rho_c\cos Y \ , \tag{A7}$$

$$v_y^i=v_c(1-\cos\theta_2)-\frac{\tilde{V}_1}{\Omega}\cosh\rho_c\sin Y \ . \tag{A8}$$

Averaging the impact energy $\varepsilon_i=\frac{1}{2}(v_x^2+v_y^2)$ over Y, assuming uniform density, it follows that

$$\langle\varepsilon_i\rangle=\left[v_c\frac{4\tilde{V}_1}{\Omega}\sinh\rho_c+\frac{\tilde{V}_1^2}{4\Omega^2}\sinh^2\rho_c+\sqrt{4\pi v_c}\left[\frac{\tilde{V}_1}{\Omega}\sinh\rho_c\right]^{3/2}+\frac{1}{4}\left[\frac{2\pi\tilde{V}_1}{\Omega}\sinh\rho_c\right]^2+\frac{1}{4}\frac{\tilde{V}_1^2}{\Omega^2}\cosh^2\rho_c\right] \ . \tag{A9}$$

Given that $\tilde{V}_1\sinh\rho_c/\Omega$ is a small quantity (typically <0.10 at full power), the dominant contribution comes from the first-order term in $\tilde{V}_1$:

$$\varepsilon_i=4\frac{E_c}{\Omega^2}\tilde{V}_1\sinh\rho_c \ . \tag{A10}$$

The second-order terms become important when $E_c \simeq 0$, since then v_c goes to zero, and

$$\varepsilon_i=\frac{\tilde{V}_1^2}{2\Omega^2}\cosh^2\rho_c \ . \tag{A11}$$

The effects of the space charge are introduced by replacing ρ and Ω in Eqs. (A10) and (A11) with $\tilde{\rho}$ and $\tilde{\Omega}$, respectively.

APPENDIX B: FLIGHT TIME

To determine the density $n(X;y)$ and the current $I(X;y)$, we need the flight time τ. In general, τ is a function of both coordinates of the original d, Y_0 and present position X, Y of the fluid element:

$$\tau_0(X,Y)=\Omega\int_d^X\frac{dX'}{\{\tilde{V}_1^2\sinh^2X'-[U_0+\Delta\mathcal{V}_0(X')]^2\}^{1/2}} \ , \tag{B1}$$

where $U_0=V_1\sinh d \sin y_0+\Delta\mathcal{V}_0(d)$, and Y_0 is related to Y through

$$\sin Y_0=\sin Y\frac{\sinh X}{\sinh d}+\frac{\Delta\mathcal{V}_0(X)-\Delta\mathcal{V}_0(d)}{\tilde{V}_1\sinh d} \ . \tag{B2}$$

One can, however, define some average flight time $\tau(X)$, by requiring current conservation:

$$\int dY\, n_0(y-v_p\tau_0(X,Y))\frac{\tilde{V}_1}{\Omega}\sinh X\cos Y = n_0(\bar{y}(X))\int dY\frac{\tilde{V}_1}{\Omega}\sinh X\cos Y \ . \tag{B3}$$

A first-order expansion of both sides in τ and τ_0 results in

$$\tau(X)=\frac{\int_{Y_1}^{Y_2}dY\,\tau_0(X,Y)\cos Y}{\sin Y_2-\sin Y_1} \ , \tag{B4}$$

where $\tau_0(X,Y)$ is given by (B1).

APPENDIX C: EFFECT OF CYCLOTRON CURRENT

It is proven here that the energy exchange between the rf wave and the cyclotron part of the electron motion is zero for uniform gyroangle distribution around each guiding center. The total electron velocity is $\mathbf{v}=\mathbf{U}+\mathbf{v_c}$, where $\mathbf{U}$ given in Eq. (20) includes both the dc and the rf drifts, and $\mathbf{v_c}$ is the gyration (cyclotron) velocity. Note that since $\mathbf{U}$ depends only on the local fields at the guiding-center location, any thermal spreads appear in the cyclotron velocity. The phase space can be completely specified by the guiding-center coordinates (X, Y), the cyclotron velocity $v_c \equiv |\mathbf{v_c}|$, and the gyroangle θ, in place of the usual coordinates and velocities x, y, v_x, and v_y. The electron distribution in phase space $F(x,y,v_x,v_y)$ is thus expressed as

$$F(X,Y,v_c,\theta)=n(X,Y)f(v_c,\theta) \ . \tag{C1}$$

The GC velocity $\mathbf{U}$ does not enter the distribution as an independent variable, since it is completely specified by

the particle's GC position. The two expressions for $\mathbf{J}\cdot\mathbf{E}_1$,

$$n(x,y)\int_{-\infty}^{\infty}dv_x\int_{-\infty}^{\infty}dv_y f(v_x,v_y)\mathbf{v}\cdot\mathbf{E}(x,y,t) \tag{C2}$$

and

$$n(X,Y)\int_0^{\infty}dv_c v_c\int_0^{2\pi}d\theta\, f(v_c,\theta)(\mathbf{U}+\mathbf{v}_c)\cdot\mathbf{E}(x,y,t)\ , \tag{C3}$$

are fully equivalent. For a uniform distribution around each GC,

$$f(v_c\theta)=\frac{1}{2\pi}f_0(v_c)\ , \tag{C4}$$

the cyclotron current contribution to the energy exchange is

$$\mathbf{J}_c\cdot\mathbf{E}_{rf}=n(X,Y)\int_0^{\infty}dv_c v_c\int_0^{2\pi}d\theta\frac{1}{2\pi}f_0(v_c)\mathbf{v}_c\cdot\mathbf{E}(x,y,t)\ . \tag{C5}$$

One could now expand $x=X+(v_c/\Omega)\sin(\theta)$ $y=Y+(v_c/\Omega)\cos\theta$ in the argument of the electric field, and take the θ-average term by term. A direct and more elegant approach is to notice that

$$\int_0^{2\pi}d\theta\,\mathbf{v}_c=\Omega\oint\mathbf{dl}\ , \tag{C6}$$

where $\oint$ is the circumference of a circle of radius $\rho=v_c/\Omega$. Then, according to Stoke's identity,

$$\int_0^{2\pi}d\theta\,\mathbf{v}_c\cdot\mathbf{E}=\Omega\oint\mathbf{dl}\cdot\mathbf{E}=\Omega\int(\nabla\times\mathbf{E})\cdot\mathbf{d}\sigma\ , \tag{C7}$$

where the surface integral is taken over the area of a circle of radius ρ. The last term is zero for the electrostatic approximation $\nabla\times\mathbf{E}=0$; thus for uniform θ-distribution

$$\mathbf{J}_c\cdot\mathbf{E}=0\ . \tag{C8}$$

This result holds for any time or space dependence of $\mathbf{E}$. In particular, it is true for any wavelength-to-gyroradius ratio λ/ρ. A uniform distribution in θ is the statistically most probable distribution in the absence of cyclotron resonances and relativistic bunching effects.

APPENDIX D: EVALUATION OF MEAN-FIELD PARAMETERS

The mean-field rf potential is parametrized by $\hat{\Lambda}$ and $\hat{\psi}$. We must define these parameters so that the para-potential flow $\mathbf{u}=-c\nabla\hat{\mathcal{V}}_1\times\mathbf{B}/B^2$ resulting from the mean field is the best match to the exact flow $\mathbf{u}=-c\nabla\mathcal{V}_1\times\mathbf{B}/B^2$. Thus $\hat{\Lambda}$ and $\hat{\psi}$ are obtained from the minimization of

$$I=\int_0^D dX\int_0^{2\pi}dY\{\hat{\mathbf{z}}\times[\nabla\mathcal{V}_1(X,Y)-\nabla\hat{\mathcal{V}}_1(X,Y;\hat{\Lambda},\hat{\psi})]\}^2\ . \tag{D1}$$

Equation (D1) is also written as

$$I=\int_0^D dX\int_0^{2\pi}dY(|\hat{\mathbf{E}}_y-\mathbf{E}_y|^2+|\hat{\mathbf{E}}_x-\mathbf{E}_x|^2)^2\ , \tag{D2}$$

where

$$\begin{aligned}
-E_x&=\tilde{V}_1[1+\epsilon_1'(X)]\cosh X\sin Y\\
&\quad+V_1\epsilon'_{-1}(X)\cosh X\cos Y\ ,\\
-E_y&=\tilde{V}_1[1+\epsilon_1(X)]\sinh X\cos Y\\
&\quad-V_1\epsilon_{-1}(X)\sinh X\sin Y\ ,\\
-\hat{E}_x&=\hat{\Lambda}\tilde{V}_1\cosh X\sin(Y+\hat{\psi})\ ,\\
-\hat{E}_y&=\hat{\Lambda}\tilde{V}_1\sinh X\cos(Y+\hat{\psi})\ ,
\end{aligned}$$

and we have defined

$$\begin{aligned}
\epsilon_{\pm1}(X)&=\frac{\delta\mathcal{V}_{\pm1}(X)}{\tilde{V}_1\sinh X}\ ,\\
\epsilon'_{\pm1}(X)&=\frac{\frac{d}{dX}\delta\mathcal{V}_{\pm1}(X)}{\tilde{V}_1\cosh X}\ .
\end{aligned} \tag{D3}$$

After integration over Y, Eq. (D2) becomes

$$\begin{aligned}
I=\tilde{V}_1^2\int_0^D dX-\{[1+\epsilon_1'(X)]\cos\hat{\psi}+\epsilon'_{-1}(X)\sin\hat{\psi}\}\hat{\Lambda}\cosh^2X-\{[1+\epsilon_1(X)]\cos\hat{\psi}+\epsilon_{-1}(X)\sin\hat{\psi}\}\hat{\Lambda}\sinh^2X\\
+\tfrac{1}{2}\hat{\Lambda}^2[\sinh^2X+\cosh^2X]+\tfrac{1}{2}[1+\epsilon_1'(X)]^2\cosh^2X+\tfrac{1}{2}[1+\epsilon_1(X)]^2\sinh^2X+\tfrac{1}{2}[\epsilon^2_{-1}(X)+\epsilon'^2_{-1}(X)]\ .
\end{aligned} \tag{D4}$$

Expression (D4) has an extremum at $\hat{\Lambda}_0$, $\hat{\psi}_0$ if $\partial I/\partial\hat{\Lambda}=0$, $\partial I/\partial\hat{\psi}=0$. Setting the partial derivatives of Eq. (D4) in $\hat{\Lambda}$ and $\hat{\psi}$ to zero leads to

$$\cos(\hat{\psi})\langle[1+\epsilon_1'(X)]\cosh^2X+[1+\epsilon_1(X)]\sinh^2X\rangle+\sin(\hat{\psi})\langle\epsilon'_{-1}(X)\cosh^2X+\epsilon_{-1}(X)\sinh^2X\rangle=\hat{\Lambda}\langle\cosh^2X+\sinh^2X\rangle\ , \tag{D5}$$

$$\sin(\hat{\psi})\langle[1+\epsilon_1'(X)]\cosh^2X+[1+\epsilon_1(X)]\sinh^2X\rangle=\cos(\hat{\psi})\langle\epsilon'_{-1}(X)\cosh^2X+\epsilon_{-1}(X)\sinh^2X\rangle\ , \tag{D6}$$

where $\langle\ \rangle\equiv\int_0^D dX$. Solution of the system (D5) and (D6) and use of the trigonometric relations $\cos(\hat{\psi})=1/\sqrt{1+\tan^2\hat{\psi}}$, $\sin\hat{\psi}=\tan(\hat{\psi})/\sqrt{1+\tan^2\hat{\psi}}$ yield the values

$$\hat{\psi}_0=\tan^{-1}\left[\frac{\langle\epsilon_1\sinh^2X+\epsilon_1'\cosh^2X\rangle}{\langle(1+\epsilon_1)\sinh^2X+(1+\epsilon'_{-1})\cosh^2X\rangle}\right]\ , \tag{D7}$$

$$\hat{\Lambda}_0=\frac{[\langle\epsilon_1\sinh^2X+\epsilon_1'\cosh^2X\rangle^2+\langle(1+\epsilon_1)\sinh^2X+(1+\epsilon'_{-1})\cosh^2X\rangle^2]^{1/2}}{\langle\sinh^2X+\cosh^2X\rangle}\ . \tag{D8}$$

If we recast Eq. (D7) as $\tan\hat{\psi}_0 = A/B$, we find from Eqs. (D5) and (D6) that

$$\frac{\partial^2 I}{\partial \hat{\Lambda}_0^2} = \langle \cosh^2 X + \sinh^2 X \rangle > 0 , \tag{D9}$$

$$\frac{\partial^2 I}{\partial \hat{\psi}_0^2} = \hat{\Lambda}(B\cos\hat{\psi}_0 + A\sin\hat{\psi}_0) = \hat{\Lambda}\sqrt{A^2+B^2} > 0 , \tag{D10}$$

$$\frac{\partial^2 I}{\partial \hat{\Lambda}_0 \partial \hat{\psi}_0} = B\sin\hat{\psi}_0 - A\cos\hat{\psi}_0 = 0 . \tag{D11}$$

From Eqs. (D9)–(D11), it follows that $\hat{\Lambda}_0$ and $\hat{\psi}_0$ *minimize* I and thus give the best approximation to the exact parapotential flow.

[1] N. Kroll, in *Microwave Magnetrons,* edited by G. B. Collins (McGraw-Hill, New York, 1948), Ch. 2, p. 49.
[2] R. C. Fletcher, Proc. IRE **40**, 951 (1952).
[3] J. Walling, J. Electron. **3**, 239 (1957).
[4] O. Buneman, in *Cross Field Microwave Devices,* edited by E. Okress (Academic, New York, 1961), p. 367.
[5] G. Mourier, in *Cross Field Microwave Devices* (Ref. [4]), p. 395.
[6] R. C. Davidson, K. T. Tsang, and J. A. Swegle, Phys. Fluids **27**, 2332 (1984).
[7] R. C. Davidson and K. T. Tsang, Phys. Fluids **28**, 1169 (1985).
[8] R. C. Davidson, Phys. Fluids, **28**, 1937 (1985).
[9] G. E. Dombrowski, IEEE Trans. Electron Devices **ED-6**, 419 (1959).
[10] R. M. Vaughan, IEEE Trans. Electron Devices **ED-20**, 818 (1973).
[11] P. L. Kapitza, in *Collected Papers of P. L. Kapitza,* edited by D. ter Haar (Pergamon, New York, 1965), Vol. 2, pp. 838–871.
[12] J. Feinstein, in *Cross Field Microwave Devices* (Ref. [4]), p. 554.
[13] S. Riyopoulos, Phys. Fluids B **3**, 3505 (1991).
[14] S. Riyopoulos, D. Chernin, and A. Drobot, IEEE Trans. Electron Devices **ED-39**, 1529 (1992).
[15] S. Riyopoulos, IEEE Trans. Plasma Sci. **PS-20**, 360 (1992).
[16] S. Riyopoulos, J. Plasma Phys. **46**, 473 (1991).
[17] R. M. Vaughan, IEEE Trans. Electron Devices **ED-36**, 1963 (1989).
[18] S. P. Yu, G. P. Kooyers, and O. Buneman, J. Appl. Phys. **36**, 2550 (1965).
[19] G. E. Dombrowski, IEEE Trans. Electron Devices **ED-35**, 2060 (1988).